

**NOvA Test Beam detector calibration**

**Technical Note**

Róbert Králik<sup>1</sup>

<sup>1</sup>University of Sussex, Brighton, UK

November 9, 2023

**Abstract**

The NOvA Test Beam detector calibration uses the same calibration procedure as the standard NOvA detectors. The main aim is to remove differences in energy deposition within the detector and to provide an absolute energy scale from collected charge to physical energy units. This allows for a direct comparison of the deposited energy in the Test Beam detector with the standard NOvA detectors. On top of that, the unique qualities of Test Beam allow us to use the Test Beam calibration to validate the calibration process and possibly to provide a simulation-independent absolute energy scale.

# **14** Contents

<b>15</b>	<b>1</b>	<b>Introduction</b>	<b>1</b>
<b>16</b>	<b>2</b>	<b>Overview of the Test Beam detector</b>	<b>1</b>
<b>17</b>	<b>3</b>	<b>NOvA calibration process</b>	<b>5</b>
<b>18</b>	3.1	Relative calibration . . . . .	10
<b>19</b>	3.2	Absolute calibration . . . . .	11
<b>20</b>	<b>4</b>	<b>NOvA Test Beam detector calibration</b>	<b>12</b>
<b>21</b>	4.1	Fibre Brightness . . . . .	14
<b>22</b>	4.2	Threshold and shielding corrections . . . . .	15
<b>23</b>	4.3	Simulation . . . . .	16
<b>24</b>	4.4	Period 2 data . . . . .	21
<b>25</b>	4.5	Period 3 data . . . . .	27
<b>26</b>	4.6	Period 4 data . . . . .	33
<b>27</b>	4.7	Absolute calibration results . . . . .	37
<b>28</b>	4.8	Results . . . . .	38
<b>29</b>	4.9	Validation . . . . .	38
<b>30</b>	<b>5</b>	<b>Conclusion</b>	<b>39</b>
<b>31</b>	<b>References</b>		<b>54</b>

## 32 1 Introduction

33 The NOvA Test Beam experiment aims to improve NOvA's sensitivity to the neutrino oscillation  
34 parameters by improving our understanding of particle interactions and energy deposition  
35 in the NOvA detectors, with the hope of reducing the total systematic uncertainty by about 10%  
36 [1].

37 Specifically, Test Beam allows us to study the response of tagged single particles as a function  
38 of their measured energies and compare it to the simulated prediction. It also enables us to  
39 determine the energy resolution and the absolute energy scale of these particles. Additionally,  
40 we are able to compare the response of beam and cosmic ray muons, to study fibre attenuation,  
41 or to validate the entire NOvA calibration process. Test Beam detector was also equipped with  
42 a combination of near and far detector readout electronics and filled with a variety of NOvA  
43 scintillator oils, which makes it possible to make a comparison of their responses [2].

44 All the aforementioned benefits of running the NOvA Test Beam experiment require, or  
45 benefit from, the Test Beam detector calibration.

46 The Test Beam detector calibration was first pioneered by Kevin Moulder who adapted the  
47 NOvA calibration codebase for Test Beam and tested it on period 1 Test Beam data [3]. This  
48 was followed by Anna Hall who improved it and got the first usable calibration of the Test  
49 Beam detector based on the period 2 data [4]. Lastly, Rober Kralik took over and finished the  
50 Test Beam calibration with help from Randeeth Dasanayaka with all Test Beam data and a new  
51 simulation in 2023 [5].

## 52 2 Overview of the Test Beam detector

53 The NOvA Test Beam detector is a scaled down version of the near and far detectors shown on  
54 figure 1. It is placed in the MC7b enclosure of the Fermilab Test Beam Facility in the path of  
55 the MCcenter beamline with a variety of beamline detectors to measure and identify a range of  
56 particles with various momenta [6].

57 The Test Beam detector started with commissioning runs in June 2019 and ran, with an  
58 exception of regular summer shutdowns, until July 2022, after which it was decommissioned.  
The Test Beam data periods are:

Period 1	June 3 <sup>rd</sup> 2019	-	July 6 <sup>th</sup> 2019
Period 2	December 5 <sup>th</sup> 2019	-	March 20 <sup>th</sup> 2020
Period 3	January 12 <sup>th</sup> 2021	-	June 27 <sup>th</sup> 2021
Period 4	November 30 <sup>th</sup> 2021	-	July 10 <sup>th</sup> 2022

Table 1: Test Beam detector data taking periods.

59  
60 Majority of the Test Beam detector and its instrumentation is identical to the other NOvA  
61 detectors, with a few exceptions that could have an impact on the calibration. We are going to  
62 identify and discuss these differences in this section.

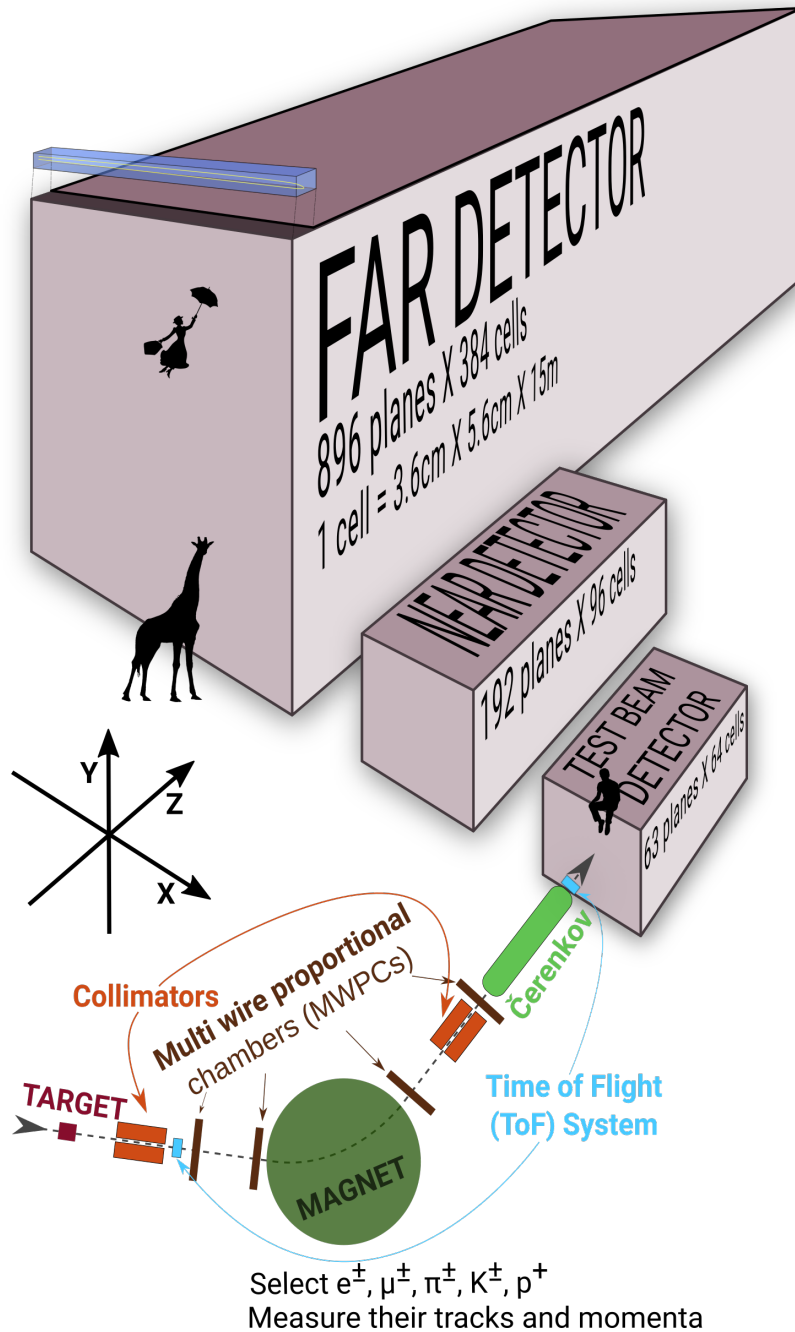


Figure 1: Comparison of Test Beam detector scale to the Near and Far NOvA detectors (and a man, giraffe, or Mary Poppins). Also shown are the Test Beam beamline detectors and components (not to scale), with arrows showing the direction of the beam. The three black arrows show the orientation of the detector coordinate system.

### <sup>63</sup> General parameters

- <sup>64</sup> The NOvA Test Beam detector consists of two 31-plane blocks, each beginning and ending  
<sup>65</sup> with a vertical plane, with an additional horizontal plane glued in-between them to preserve  
<sup>66</sup> the alternating pattern [7]. Each plane consists of 2 modules side-by-side, both made up of 32

67 cells. Each cell is 2.6 m long with an inner (without the PVC) depth and width of 5.9 cm and  
68 3.8 cm respectively, same as for the other NOvA detectors. This brings the final dimensions of  
69 the Test Beam detector to 63 planes  $\times$  64 cells, or  $2.6 \times 2.6 \times 4.1 \text{ m}^3$ .

70 The 63 planes are numbered from 0 to 62, with even numbers corresponding to vertical  
71 planes and odd numbers to horizontal planes. Cells are numbered 0 to 63, going from bottom  
72 to top for horizontal planes and left to right, when facing the front of the detector, for vertical  
73 planes.

74 The detector coordinate system is illustrated on figure 1. It is centred with (0,0,0) in the  
75 centre of the first plane [8]. The x axis runs left to right when facing the front of the detector,  
76 y axis bottom to top, and z axis goes along the beam direction from front to the back of the  
77 detector. Position within each cell ( $w$ ) is aligned with the x (y) axis for the horizontal (vertical)  
78 cells, with  $w = 0$  centred in the middle of each cell. The exact geometry of the Test Beam  
79 detector was measured in several alignment surveys and is saved in gdml files [9].

80 In the past we encountered an issue when trying to align the Test Beam detector with the  
81 beamline measurements by rotating the detector. This broke several assumptions within the  
82 Test Beam geometry [8] and manifested as uncalibrated cells in the back of the detector [10].  
83 This was fixed by realigning both the detector and the beamline separately, based on the last  
84 alignment survey, measured during the decommissioning of the detector. We implemented the  
85 fix in the production tag R23-04-05-testbeam-production.a [8].

## 86 Scintillator

87 Test Beam used a combination of the leftover near and far detector production scintillator oils  
88 and the oil drained from the NDOS test detector. The used scintillator oils also differ in the  
89 way they were stored since the filling of the near and far detectors, or NDOS draining, which  
90 apparently impacted its quality. The distribution of individual scintillator oils and the relative  
91 difference in their energy response can be seen on figure 2.

92 We can distinguish four samples of the NOvA scintillator oil used in the Test Beam detector:

- 93 • Mixed near detector production oil and NDOS-drained oil stored in a tanker and tanks  
94 outside in Fermilab [11];
- 95 • Separate near detector production oil and NDOS-drained oil stored underground in barrels  
96 at MiniBooNE [1];
- 97 • Far detector production oil stored inside in Ash River in "totes" under several layers of  
98 black plastic [12];
- 99 • NDOS-drained oil stored mainly inside at Texas A&M University and University of  
100 Texas at Austin [13, 14].

101 The original plan [15] was to only use the tanker/tank scintillator (sample 1). First tests  
102 showed acceptable results and the tanker oil was used to fill out almost the entirety of the first  
103 block of the detector (first 32 planes) [11]. However, when we loaded oil from tank two into  
104 the tanker, it became extremely cloudy and unusable, possibly due to contamination with water  
105 accumulated at the bottom of the tanks. The rest of the first block was therefore topped up with  
106 high quality scintillator from NDOS (sample 2). This is labelled as "Fermilab ND+NDOS oil"  
107 on figure 2.

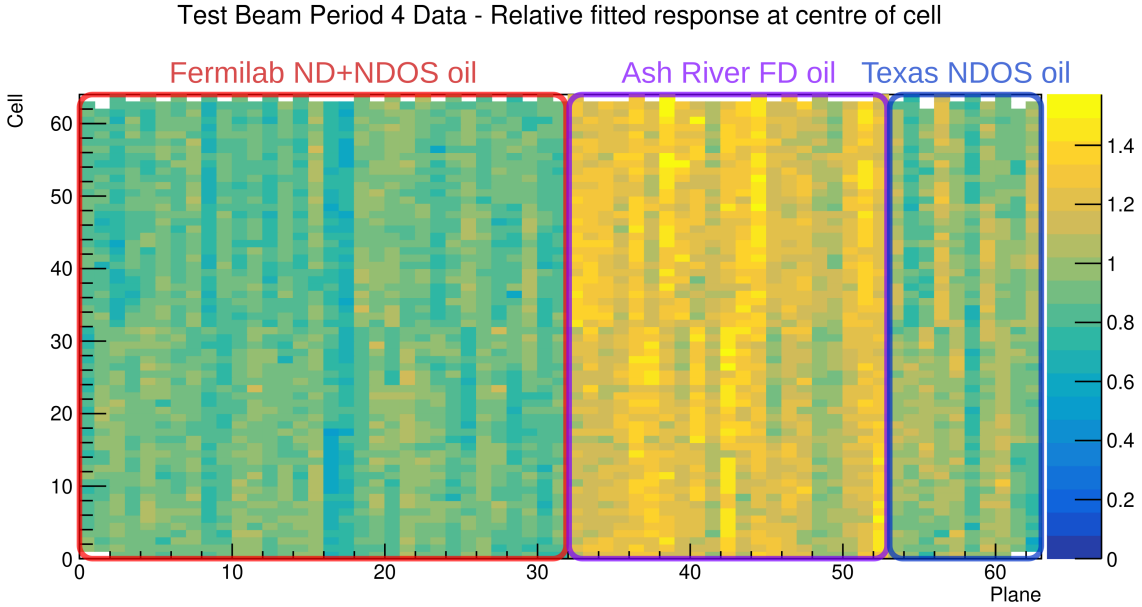


Figure 2: Uncorrected energy response in the centre of cells across the Test Beam detector showing a clear distinction between the different scintillator oils, shown with coloured boxes.

The first 21 planes of the second block (planes 32 to 52) were filled with the far detector production scintillator shipped in from Ash River (sample 3) [16]. We again topped up these planes with the ND+NDOS scintillator (sample 2) [16].

The last 10 planes (planes 53 to 62) [16] were filled with the "Texas" scintillator (sample 4), which has higher light yield than the one from the tanker, but lower than the Ash River one [13].

In total the Test Beam detector is filled with 5418 gallons of scintillator oil with a weight of approximately 28.6 tons [7].

## 116 **Readout**

The Test Beam detector uses in total 126 Front End Boards (FEBs), each reading out signal from 32 cells (one module = half of a plane) [7]. The readout is located on the top and right side (when looking at the front) of the detector. 118 FEBs are version 4.1, same as in the Far Detector, and 8 FEBs, located in pairs on planes 16, 17, 48 and 49, are version 5.2, same as in the Near Detector. The Near Detector FEBs are designed to read out data in a faster rate and we used a mix of FEB types to study the difference in their response and to validate both versions in the same environment [17].

## 124 **Environment**

Unlike the near and the far detector, the Test Beam detector does not have any overburden to shield it from cosmic particles, which affects their rate and energies inside the detector. There is also less precise control of temperature and humidity than in the other detectors [source?], which can potentially impact the scintillator and readout performance.

129 **Underfilled cells issue**

130 The Test Beam detector is slightly tilted around the Z axis by about  $0.7^\circ$  towards the readout.  
131 This caused the top cells of both modules of all the horizontal planes (cells 31 and 63) to be  
132 underfilled, creating an air bubble on the left side of the detector and severely affecting the  
133 energy response in those cells [17]. This has been fixed [18] during the period 3 running by  
134 adding extensions to the filling ports and overfilling the horizontal cells with the ND+NDOS  
135 scintillator (sample 2).

136

### 3 NOvA calibration process

137 Test Beam is following the same ideas and procedures as the standard NOvA calibration. This  
138 section intends to provide only a brief overview of the NOvA calibration, with further details  
139 in the range of NOvA calibration technical notes [19]. All the code required for calibration is  
140 located in the NOvASoft Calibration package and the outline of the files and processes in  
141 NOvA calibration are shown on figure 3.

142 The purpose of calibration is to make sure that we get the same amount of energy wherever  
143 or whenever it's deposited in whichever of NOvA's detectors and to express this amount of  
144 energy in physical units. The NOvA calibration uses cosmic ray muons, which provide a  
145 consistent, abundant, and well-understood source of energy deposition and consists of two  
146 parts [20]:

- 147 1. The **relative calibration** corrects for attenuation of scintillator light as it travels through  
148 the cell to the readout, as well as for differences between detector cells. This correction  
149 is calculated for each cell separately.
- 150 2. Followed by the **absolute calibration**, which only uses stopping muons when they are  
151 minimum ionising particles. In the absolute calibration we calculate a scale between  
152 the measured energy deposition, corrected by the relative calibration, and the simulated  
153 energy deposition in physical units of MeV. This scale is calculated for each time period  
154 and each detector separately, which ensures the energy deposition is directly comparable  
155 wherever or whenever it occurred.

156 The NOvA calibration process technically also involves **timing calibration**, which corrects  
157 for the time differences of the signal to be processed [21]. However, this is done as a separate  
158 project to the relative and absolute calibrations and is out of scope of this technical note.

159 The basic units and variables used to define energy deposited in the NOvA detectors are  
160 listed in table 2.

The final result of the NOvA calibration is the deposited energy in terms of physical units,

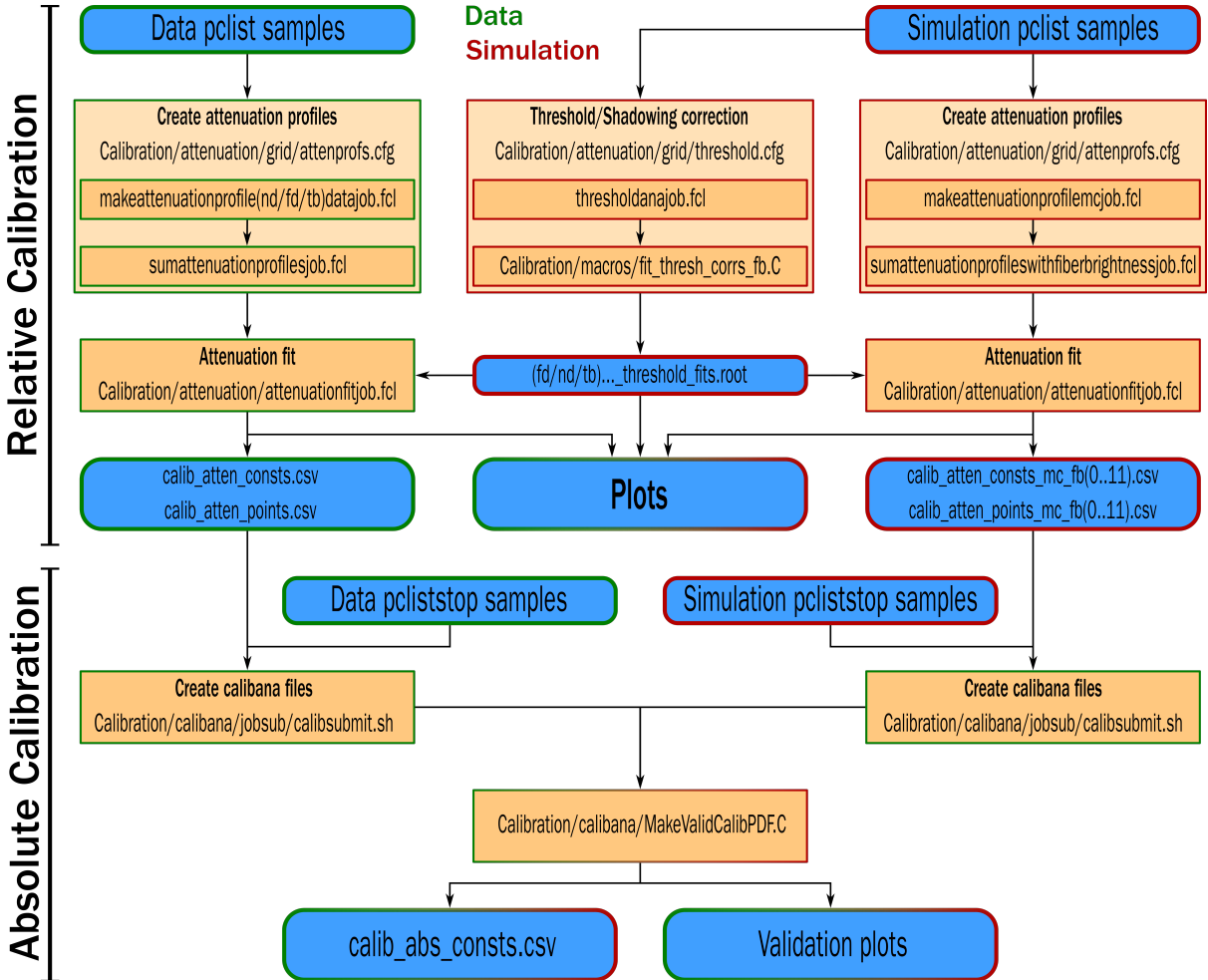


Figure 3: Flow chart showing the jobs (orange background) and files (blue background) needed and produced during the full NOvA calibration process. The left chain is showing the data calibration process (with green border) and is applied to every data calibration sample separately (periods or epochs). The center and right chains are showing the simulation calibration process (red border), which is redone only if there's a change to the detector simulation. The absolute calibration at the bottom combines data and simulation. The entire process is done separately for each NOvA detector.

ADC	The digitized charge collected by the APDs from the Analog to Digital Converter [22].
PE	Number of Photo Electrons. Calculated by a simple rescaling of the best estimate of the peak ADC. The PE per ADC scale only depends on the FEB type and the APD gain settings. This conversion is done before the calibration and PE serves as the base unit for calibration.
PECorr	Corrected PE after applying the relative calibration results. The correction is a ratio between an average energy response (a pre-determined semi-arbitrary number) and the result of the the relative calibration fit (also called attenuation fit), which depends on w, cell, plane, epoch and detector. This makes the energy response equivalent across each detector.
MEU	Muon Energy Unit is the mean detector response to a stopping cosmic minimum ionising muon. For true variables it's equivalent to the mean MeV/cm and for reconstructed variables to the mean PECorr/cm.
MeV	Estimated energy deposited in the scintillator calculated from PECorr using the results of the absolute calibration. Additional correction for dead material needs to be made in order to get an estimate of the calorimetric energy.

Table 2: Definitions of variables commonly used in calibration [19, 20].

which is in effect calculated as:

$$E_{dep}[\text{MeV}] = \underbrace{\frac{\text{MEU}_{truth}[\text{MeV}/\text{cm}]}{\text{MEU}_{reco}[\text{PECorr}/\text{cm}]}}_{\substack{\text{Absolute calibration} \\ (\text{Detector, epoch})}} \times \underbrace{\frac{\text{Average response}[\text{PECorr}]}{\text{Fitted response}[\text{PE}]}}_{\substack{\text{Relative calibration} \\ (\text{Detector, epoch, plane, cell, w})}} \times \underbrace{\left[ \frac{\text{PE}}{\text{ADC}} \right]}_{\substack{\text{Scale} \\ (\text{APD Gain, FEB})}} \times \text{Signal}[\text{ADC}], \quad (1)$$

where both the relative calibration results (blue fraction) and the absolute calibration results (red fraction) are stored in a database and applied together with the ADC-to-PE scale by the NOvAsoft Calibrator package during processing of every hit in the NOvA detectors.

#### Creating calibration samples

We want to select good quality cosmic ray muons. First, we remove beam related events based on their time stamps relative to the time of the beam spill, using the RemoveBeamSpills (for the near and far detectors), or RemoveTBSpills filter (for the Test Beam detector), as shown on figure 4. Next we apply reconstruction to get the CellHit, slicer, and track information, followed by a track-based selection to remove misreconstructed and poor quality events.

Since energy deposition depends on the path length particle travels through a cell, we only use hits for which we can reliably calculate their path length. We call these hits **tricell** hits, as we require that all accepted hits are accompanied by a recorded hit in both neighbouring cells of the same plane, as shown on figure 5. In case there is a bad channel in a neighbouring cell,

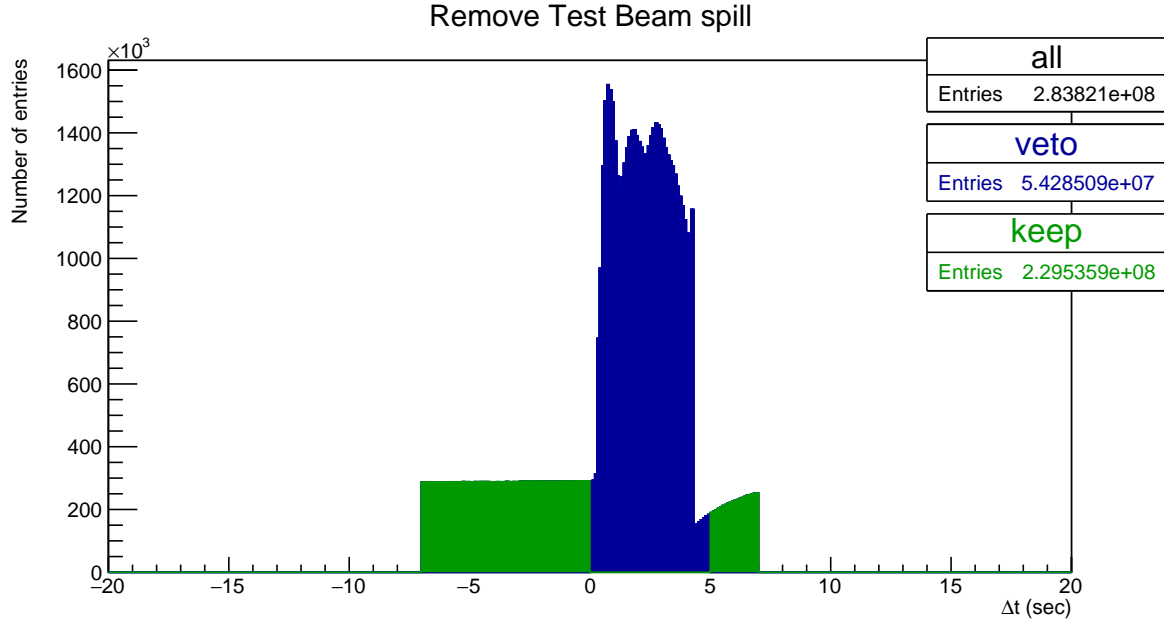


Figure 4: Test Beam beam spill events removed from the calibration samples. Test Beam beam spill is 4.2 seconds long and we remove events (in blue) within a 5 seconds window from the start of the beam spill. The remaining events (green) should mostly consist of cosmic particles. This example and the numbers of entries are for the full period 4 Test Beam sample.

<sup>174</sup> we ignore this channel and look one cell further. We can then calculate the path length simply  
<sup>175</sup> as the cell width divided by the cosine of the direction angle [19, 20].

<sup>176</sup> For the absolute calibration we select muons that stop inside the detector, by identifying  
<sup>177</sup> muons with a Michel electron at the end of their track [23].

<sup>178</sup> For each data period or epoch and for each version of the simulation we create two calibra-  
<sup>179</sup> tion samples that are used as the input for the relative and absolute calibration. The samples  
<sup>180</sup> are called [24]

- <sup>181</sup> • pclist = **list** of pre-calibrated hist; Contains all selected cosmic muon events and is used  
<sup>182</sup> in the relative calibration;
- <sup>183</sup> • pcliststop = pclist files only containing stopping muons used for the absolute calibration

#### <sup>184</sup> Fibre brightness

<sup>185</sup> For data, the relative calibration is done for each individual cell in each plane to properly  
<sup>186</sup> account for any potential variations, repeating the attenuation fit  $N_{cell} \times N_{plane}$  times. However,  
<sup>187</sup> generating enough simulated events turned out to be computationally expensive. Therefore,  
<sup>188</sup> assuming the simulated detector is approximately uniform plane to plane, for simulation we  
<sup>189</sup> can "consolidate" the detector planes and only consider variations in the two views. Therefore  
<sup>190</sup> for simulation we would repeat the fit  $N_{cell} \times N_{view}$  times [25, 26].

<sup>191</sup> However, there are some variations in the detector response cell by cell that can be caused  
<sup>192</sup> by different fibre brightnesses, but also by different qualities of the scintillator, air bubbles,  
<sup>193</sup> APD gains, looped or zipped fibres and potentially others. We want to include these variations

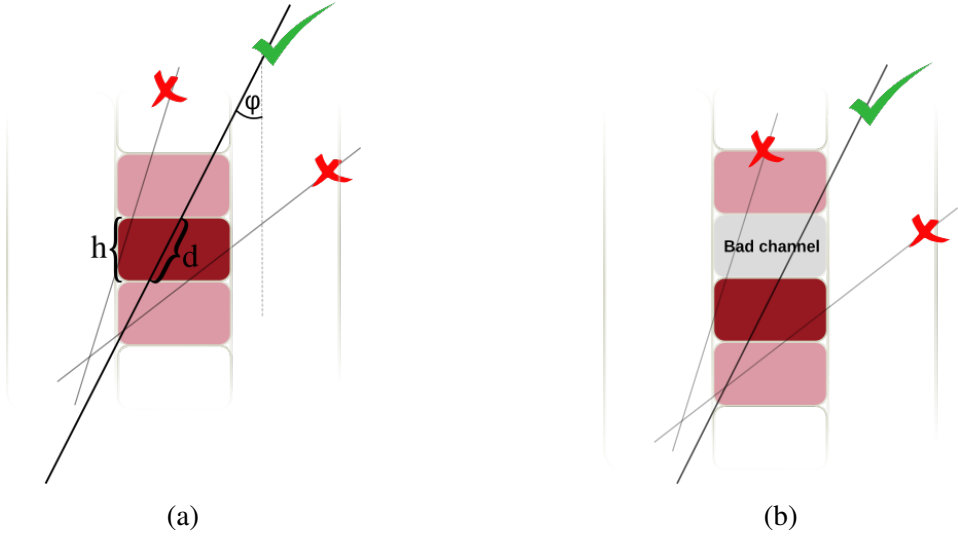


Figure 5: Illustration of the tricell condition (a). We only use hits that have two surrounding hits in the same plane to be used in the NOvA calibration. This is to ensure a good quality of the path length ( $d$ ) reconstruction, which is calculated from the known cell height ( $h$ ) and the reconstructed track angle ( $\phi$ ). In case the hit is next to a bad channel (b), we ignore this bad channel and require a hit in the next cell over.

in the simulation to better match data. To emulate these differences in the simulation without the need to simulate every cell individually, we divide each detector into 12 brightness bins, as shown on figure 6. These brightness bins describe the relative differences in the detector response between individual cells [26]. Therefore in the end, for simulation we perform the attenuation fit  $N_{cell} \times N_{view} \times N_{BrightnessBin}$  times.

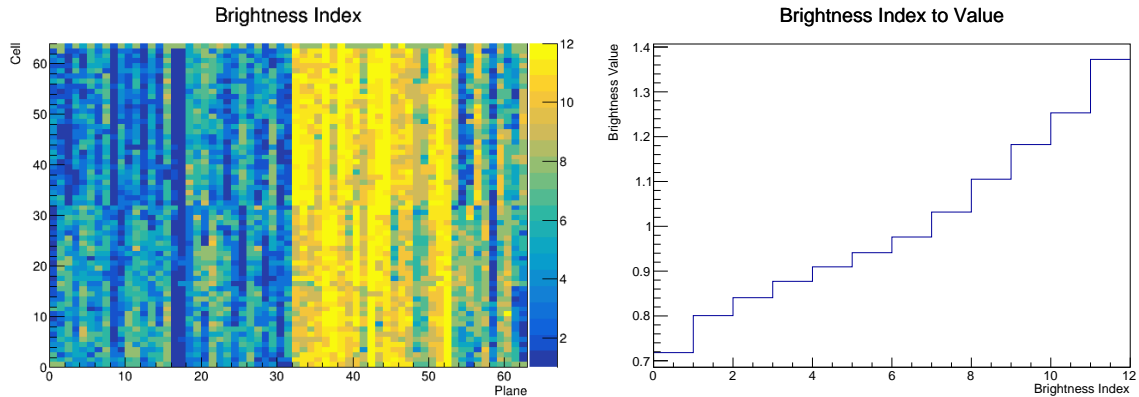


Figure 6: The Test Beam detector is (like the standard NOvA detectors) divided into 12 brightness bins (left plot), each representing a relative difference in energy response (right plot) due to different brightnesses of the fibres, scintillators, or readout.

To divide each detector into the 12 brightness bins, we use results from the relative calibration. Specifically we take the result of the attenuation fit (equal to the average response) in the centre of each cell to fill a 2D histogram. Then we normalize this histogram by dividing the response in each Cell  $\times$  View  $\times$  Plane by the average response in the corresponding

203 Cell  $\times$  View. All uncalibrated cells get assigned the average response (1 in normalized his-  
204 togram). Then we make a 1D histogram filled with the normalized responses of each cell and  
205 divide this histogram into 12 equally populated bins (so each bin represents approximately the  
206 same number of detector cells, shown on the left plot of figure 6). The mean normalized re-  
207 sponse in each bin represents the relative brightness value of this bin (right plot of figure 6).  
208 A ROOT file with the distribution of brightness bins across the detector and their correspond-  
209 ing relative brightness values is stored inside the NOvAsoft PhotonTransport package as  
210 <det>BrightnessFromCosmics.root.

211 **Threshold and shielding correction**

212 Energy deposited far away from the readout may get attenuated enough to be shifted below the  
213 threshold. These low energy depositions would be missing from the attenuation fit, biasing it  
214 towards larger light levels with increasing distance from the readout. Similar effect, specifically  
215 for the vertical cells, is caused by using cosmic muons for calibration and applying it to beam  
216 muons. The top of the detector effectively shields the bottom, skewing the energy distribution  
217 of cosmic muons. To correct for both of these effect, we use the simulation plist sample to  
218 calculate the threshold and shielding (also called threshold and shadowing) correction by com-  
219 paring the true and reconstructed information. We apply this correction before the attenuation  
220 fits [25].

221 **3.1 Relative calibration**

222 Relative calibration corrects for the attenuation of the scintillator light by fitting the average  
223 detector response over the position in each cell ( $w$ ), separately for every cell inside each de-  
224 tector. Dividing the "average response" of the detector by the result of the attenuation fit for  
225 each Plane  $\times$  Cell  $\times w$  combination effectively removes relative differences within and between  
226 all cells across the entire detector. The average response is a single constant number chosen to  
227 approximately represent the average response in the middle of the cell. Its value is for the far  
228 detector and Test Beam 39.91 PE/cm and for the near detector 37.51 PE/cm. The value of the  
229 average response has no impact of the calibration results, as the absolute scale of the detector  
230 response is determined during the absolute calibration and relative calibration only serves to  
231 remove the relative differences [20, 25].

232 To create the attenuation fit we use the following procedure [20]:

- 233 1. Create the *attenuation profiles*. Attenuation profiles are essentially profile histograms of  
234 detector response in terms of PE/cm as a function of position in the cell ( $w$ ) for each cell  
235 in all planes. We construct the attenuation profiles over a little wider range than the actual  
236 length of the cell and always with 100 bins for each detector. This means that smaller  
237 detectors, like the Test Beam detector, have a finer binning ( $\sim 3\text{cm/bin}$ ) compared to the  
238 Far Detector ( $\sim 18\text{cm/bin}$ ).
- 239 2. Analyse the attenuation profiles. The job to create the attenuation profiles also creates  
240 validation histograms, which should be analysed prior to performing the attenuation fit  
241 to make sure the attenuation profiles look as expected.
- 242 3. Apply the threshold and shielding correction that was created before the relative calibra-  
243 tion.

244 4. Do the attenuation fit over the full length of each cell. The fit consists of

- 245 (a) an exponential fit, which combines two cases. First, when the scintillating light  
travels the short distance straight to the readout, and second, when it goes to the far  
side of the cell and loops around before going to the readout. The fitted function  
has a form:

$$y = C + A \left( \exp\left(\frac{w}{X}\right) + \exp\left(-\frac{L+w}{X}\right) \right), \quad (2)$$

246 where  $y$  is the fitted response,  $L$  is the length of the cell and  $C$ ,  $A$  and  $X$  are the fitted  
parameters.  $X$  also represents the attenuation length.

- 247 (b) Smoothing of the residuals from the exponential fit, mainly at the end of cells, with  
248 the LOcally WEighted Scatter plot Smoothing (LOWESS) method.

249 5. Check the plots of the attenuation fit for a selection of cells.

250 6. Save the fit result to the database in the form of two csv tables. The `calib_atten_consts.csv`  
251 table holds the results of the exponential fit, together with the final  $\chi^2$  of the fit. The  
252 `calib_atten_points.csv` table holds the results of the LOWESS smoothing.

253 To ensure the quality of the attenuation fit, we only apply the results if the final  $\chi^2 < 0.2$ .  
254 If  $\chi^2 > 0.2$ , we ignore the results for this cell and mark it as *uncalibrated*.

## 255 3.2 Absolute calibration

256 To find the absolute energy scale, we apply the relative calibration results on the stopping  
257 muon sample and look at the energy they deposited in cells 1-2 meters from the end of their  
258 tracks. In this track window they are approximately minimum ionising particles and their  
259 energy deposition is almost constant and well understood. Additionally, we don't use hits from  
260 the edges of a cell, as those might be affected by the lower number of events, fibre endings, or  
261 loops.

262 For each calibrated data and simulation sample we take a mean of the corrected deposited  
263 energy distribution, separate for each view. We then take a simple average from the two views  
264 to get the final  $\text{MEU}_{\text{reco}}$  in units of PECorr/cm for each sample [23]. Additionally, from sim-  
265 ulation we can get the mean of the distribution of the true deposited energy in the scintillator,  
266  $\text{MEU}_{\text{truth}}$  in units of MeV/cm for the same sample of stopping muons.

267 We ignore the energy that is lost in the dead material (PVC extrusions) and deal with it sep-  
268 arately. The absolute energy scale for each sample is then the ratio of  $\text{MEU}_{\text{truth}}/\text{MEU}_{\text{reco}}$ . We  
269 save these absolute energy scales in another csv table called `calib_abs_consts.csv` which  
270 stores the MEU values and their errors.

271 As part of the absolute calibration we also produce validation plots that show the effect of  
272 calibration on the distribution of the stopping muons. We analyse these plots and if everything  
273 looks all right we load all the csv tables into the database.

## <sup>274</sup> 4 NOvA Test Beam detector calibration

<sup>275</sup> In this section we describe the details of the Test Beam detector calibration as it was finalized  
<sup>276</sup> in June 2023. This version includes a new purpose-made simulation and all measured Test  
<sup>277</sup> Beam data, with the exception of period 1 data. Period 1 only includes one month of data,  
<sup>278</sup> with half-filled detector and several issues including the beam halo [27] and was only used for  
<sup>279</sup> commissioning and is not used in any Test Beam analysis.

<sup>280</sup> The specific commands to run the Test Beam detector calibration are listed in the two  
<sup>281</sup> coloured boxes bellow, split into relative and absolute calibration steps. These steps closely  
<sup>282</sup> follow the standard NOvA calibration procedure, as described in the last section and as shown  
<sup>283</sup> on the calibration flow chart on figure 3. The most up-to-date steps and information on how to  
<sup>284</sup> run the Test Beam calibration are listed on the [Test Beam calibration redmine wiki page](#).

## Relative calibration

1. Create attenuation profiles for each data period/epoch and for simulation
  - (a) Check the parameters of fcl files in Calibration/attenuation

```
fhicl-dump makeattenuationprofiletdatajob.fcl
fhicl-dump makeattenuationprofilemcjob.fcl
```
  - (b) Submit the jobs to the grid

```
submit_nova_art.py -f Calibration/attenuation/grid/attenprofs.cfg
```
  - (c) Copy attenuation profiles to an ana area

```
ifdh cp /pnfs/nova/scratch/.../attenprof_outputs*
/nova/ana/output/dir
```
  - (d) hadd the calib hist analysis files

```
hadd -f -k calib_hist_all.root 'pnfs2xrootd
/pnfs/nova/scratch/.../calib_hist_outputs*.root'
```
  - (e) Analyse the calib\_hist\_all.root file
2. Create the Threshold/Shielding correction (if not already done)
  - (a) Create the job and the configuration script for each brightness bin

```
bash Calibration/attenuation/grid/submit_thresh_jobs.sh
```
  - (b) Rebuild the test release with novasoft\_build -t
  - (c) Create a tarball with tesrel\_tabrall <testrel> <tarball>
  - (d) Submit each config script in Calibration/attenuation/grid to the grid

```
for i in 0..11;
do submit_nova_art.py -f "threshold_fb"$i".cfg"; done;
```
  - (e) hadd the results: bash Calibration/scripts/hadd\_all\_thresh\_hists.sh
  - (f) Fit for the Threshold/Shielding correction

```
root -b -q 'Calibration/macros/fit_thresh_corrs_fb.C(
"/path/to/input/input_file_name.root",
"<name_of_the_output_threshold_file_including_tb.root>")'
```
3. Run the attenuation fit for each sample
  - (a) Check the ThresholdCorrMapFile, PlotsDirectory, and the fiberbrightness file

```
fhicl-dump Calibration/attenuation/attenuationfitjob.fcl
```
  - (b) Run the fit: nova -c attenuationfitjob.fcl -s /input/attenprof\*.root
  - (c) Carefully check all the created csv files and plots
  - (d) Copy the csv files to a pnfs area

285

## Absolute calibration

1. bash Calibration/calibana/jobsub/calibsubmit.sh -p <projectname> -t <testrel> -tar <tarballOfTestrel> -s tb\_samples.txt -relcal </path/to/csv/files/on/pnfs> -tb -data/mc -prepare/submit/check/hadd/checkhadd
  - (a) -prepare
  - (b) Rebuild the test release with novasoft\_build -t
  - (c) Create a tarball with testrel\_tabrall <testrel> <tarball>
  - (d) -submit
  - (e) -check
  - (f) -hadd
2. Update the Calibration/calibana/MakeValidCalibPDF.C with the new calibana files
3. Calculate the absolute energy scale and create the validation plots  
root -b -q 'Calibration/calibana/MakeValidCalibPDF.C(  
"tb\_Calibration\_name", "cfg/tb\_calib.cfg", "all")'  
where the first argument **must** contain "tb"
4. Carefully analyse the validation plots
5. Create a new calibration tag

287

288     The calibration samples used as inputs for the Test Beam detector calibration are listed in  
289     table 3. We are using data from one of the two Test Beam data-driven activity-based triggers  
290     (DDActivity1). To produce these samples we (or production) use the [prod\\_tb\\_ddactivity1\\_pclist\\_job.fcl](#)  
291     job from the [novaproduct/novaproduction/fcl/testbeam](#) repository, or the corresponding  
292     simulation ("mc") file. The calibration samples were originally created in keep-ups by the pro-  
293     duction, but most of them had to be reproduced in 2023 to fix a bug in the Test Beam geometry.

294     

## 4.1 Fibre Brightness

295     To divide the Test Beam detector into fibre brightness bins we used the attenuation fit results  
296     for period 4 data (described in section 4.6), as that is the best detector conditions data we have.  
297     Since we need the fibre brightness file to run the attenuation fits and we need the attenuation  
298     fit results to create the brightness file, we proceeded iteratively and first ran the attenuation fit  
299     with an older version of the brightness file and then used the newer fit results to create a new  
300     brightness file to be used in a new attenuation fit.

301     As we are only using the attenuation fit results in the centre of each cell, we've decided to  
302     allow some cells that initially failed the calibration condition ( $\chi^2 > 0.2$ ), to be still used for the  
303     creation of the brightness file. Otherwise, all the officially uncalibrated cells would be assigned  
304     an average response and we would lose the information on their relative brightness. As can be  
305     seen on figure 7, some attenuation fits have  $\chi^2 > 0.2$ , even though they correctly represent the

---

### pclist samples

---

**Data period 2:**

```
prod_pclist_R23-04-05-testbeam-production.a_testbeam_ddactivity1_period2_v1
```

**Data period 3:**

```
prod_pclist_R23-04-05-testbeam-production.a_testbeam_ddactivity1_epoch3a_v1
```

```
prod_pclist_R23-04-05-testbeam-production.a_testbeam_ddactivity1_epoch3b_v1
```

```
prod_pclist_R23-04-05-testbeam-production.a_testbeam_ddactivity1_epoch3c_v1
```

```
pclist_testbeam_detector_activity_epoch3d_R21-01-28-testbeam-production.a
```

```
pclist_testbeam_detector_activity_epoch3e_R21-01-28-testbeam-production.a
```

**Data period 4:**

```
prod_pclist_R23-04-05-testbeam-production.a_testbeam_ddactivity1_period4_v1
```

**Simulation:**

```
rkrilik_pclist_testbeam_databasedsim_R23-04-05-testbeam-production.a
```

---

### pcliststop samples

---

**Data period 2:**

```
prod_pcliststop_R23-04-05-testbeam-production.a_testbeam_ddactivity1_period2_v1
```

**Data period 3:**

```
prod_pcliststop_R23-04-05-testbeam-production.a_testbeam_ddactivity1_epoch3a_v1
```

```
prod_pcliststop_R23-04-05-testbeam-production.a_testbeam_ddactivity1_epoch3b_v1
```

```
prod_pcliststop_R23-04-05-testbeam-production.a_testbeam_ddactivity1_epoch3c_v1
```

```
pcliststop_testbeam_detector_activity_epoch3d_R21-01-28-testbeam-production.a
```

```
pcliststop_testbeam_detector_activity_epoch3e_R21-01-28-testbeam-production.a
```

**Data period 4:**

```
prod_pcliststop_R23-04-05-testbeam-production.a_testbeam_ddactivity1_period4_v1
```

**Simulation:**

```
rkrilik_pcliststop_testbeam_databasedsim_R23-04-05-testbeam-production.a
```

---

Table 3: SAMWEB definitions of the Test Beam calibration samples.

306 energy deposition in the centre of that cell. By carefully investigating all cells with  $\chi^2 > 0.2$   
307 (which is doable for Test Beam, due to its small number of cells), we concluded it is safe to use  
308 all the attenuation fit results with  $\chi^2 < 0.7$ .

309 The final distribution of brightness bins and their corresponding relative brightnesses for  
310 the Test Beam detector is shown on figure 6.

311 **4.2 Threshold and shielding corrections**

312 We created the threshold and shielding correction for Test Beam from the new simulation de-  
313 scribed in the next section 4.3. As can be seen on figure 8, the correction is almost uniform as  
314 a function of both  $w$  and cell number. This is the case for all fibre brightness bins and for both  
315 views.

316 The uniform distribution is expected, as the Test Beam detector is much smaller than the

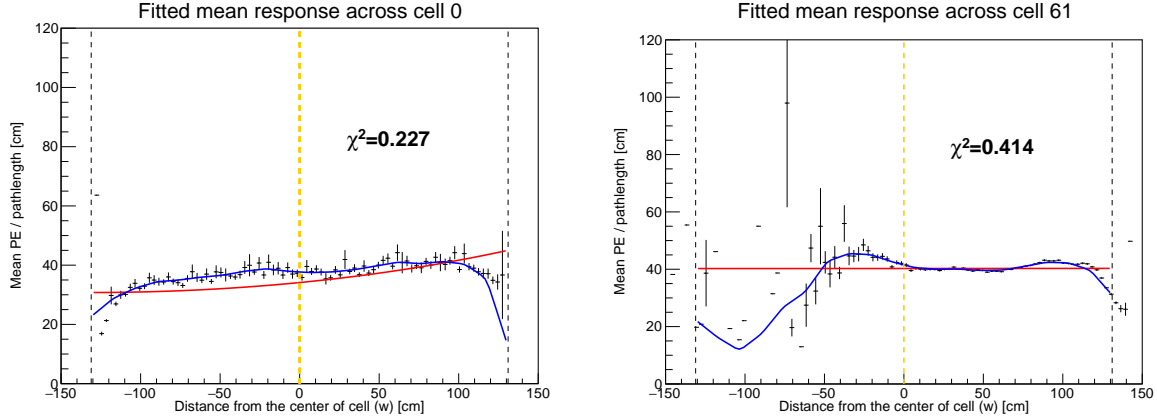


Figure 7: Attenuation fits for two cells that fail the calibration condition, but the fit (blue line) correctly represents the energy deposition in the centre of that cell (yellow dashed line).

far detector and the corrected effects don't have a significant effect. The cell length of 2.6 m has only a negligible effect on the energy distribution of cosmic muons or on the threshold saturation. Therefore the threshold and shielding correction for Test Beam is only a normalization factor, except for the cell edges, where there is a large variation in the energy response there anyway due to low number of events. Since the relative calibration only cares about relative differences across the detector, a normalization factor does not have any impact on its results.

### 4.3 Simulation

We used a custom made data-based simulation of cosmic muons for the Test Beam detector calibration. The details on the simulation and how it was created are described in the "*Data-based simulation of cosmic muons (not only) for calibration technical note*" [28]. We used half of period 4 data (used every second event as saved in the root file, therefore sampled from the entire period 4) as the inputs. We also used the newly created fibre brightness file (section 4.1) to inform the simulation on the realistic detector conditions.

The distribution of cosmic muon events from the new simulation across the detector is shown on figure 9.

An overview of the results of the attenuation fit are shown on figure 10 as a map of the response in the centre of each cell. The blank cells show the uncalibrated cells which failed the calibration condition (attenuation fit  $\chi^2 > 0.2$ ). Most of the uncalibrated cells are on the edges of the detector, which is expected as those have much fewer events that pass the calibration sample selection than the rest.

Examples of a standard detector response and of the response for cells on the edge of the detector are shown of figure 11. Here the red line shows the initial exponential fit and the blue line the final attenuation fit, after the LOWESS correction, as described in section 3.1. Most cells have an expected response with a slow rise towards the readout (right side of the plots), with drops on the edges, as shown on the top left plot.

There is only one cell in the middle of the detector that is left uncalibrated, which is the cell 32 in a vertical plane in the brightness bin 5, shown on the top right of fig. 11. The corresponding  $\chi^2 = 0.227$ . It seems the reason the  $\chi^2$  is  $> 0.2$  is the high response with a large uncertainty in the very last fitted bin.

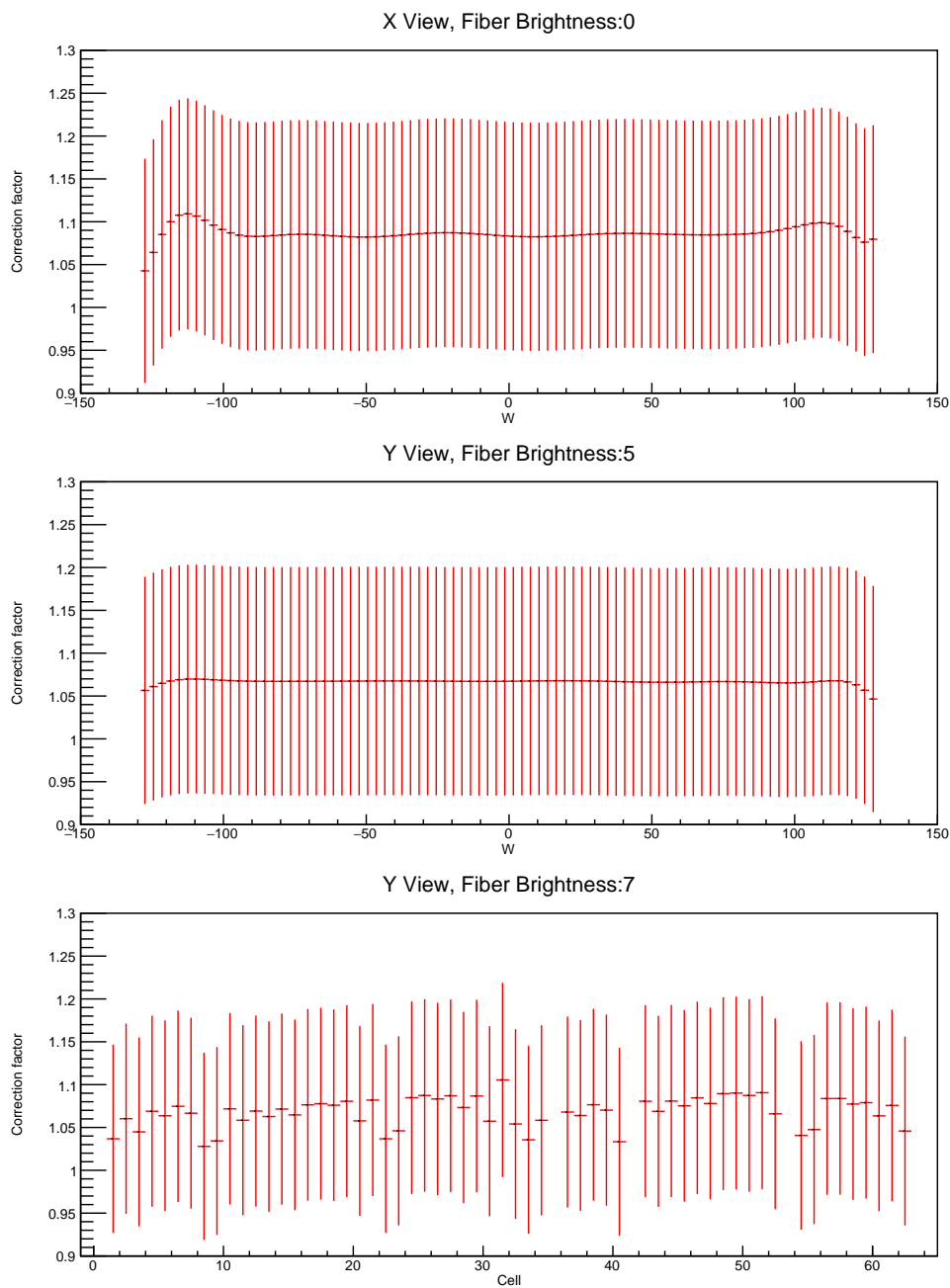


Figure 8: Examples of threshold and shielding corrections for the Test Beam detector

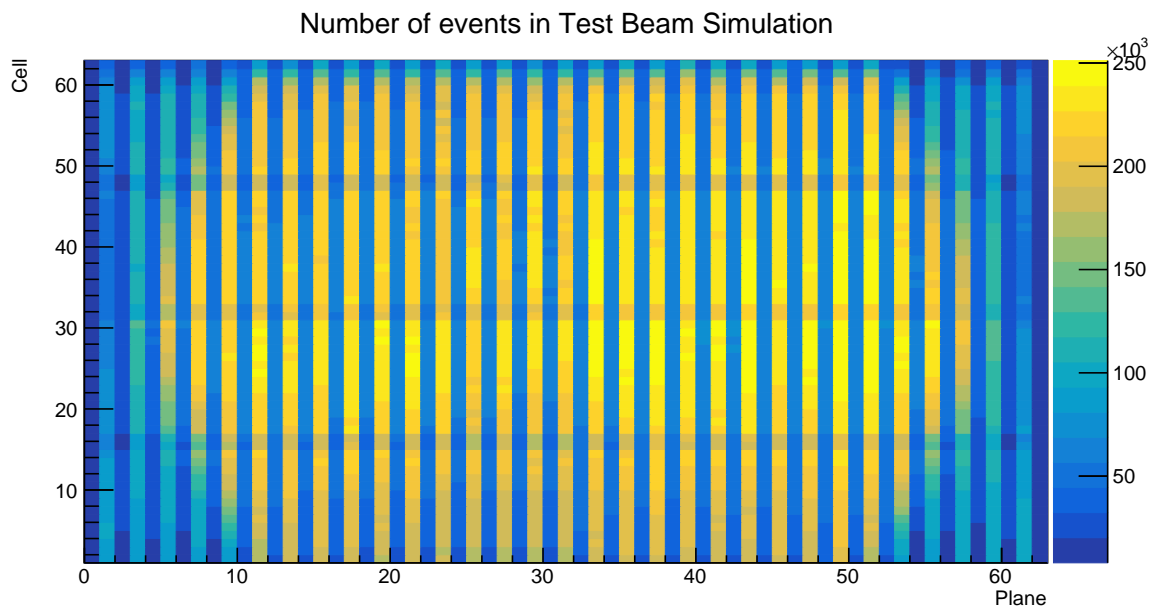


Figure 9: Distribution of events in the Test Beam simulation calibration sample.

<sup>346</sup> Overall, this is a much better result of the relative calibration (attenuation fit) for a sim-  
<sup>347</sup> ulation than any of the previous versions of the cosmic muon simulations in the Test Beam  
<sup>348</sup> detector.

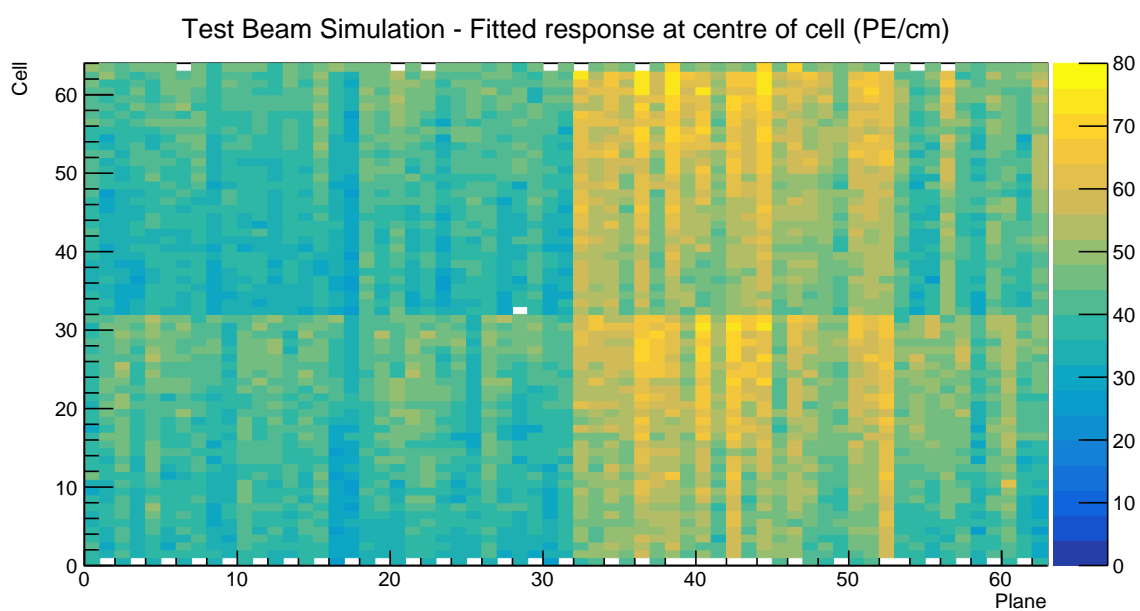


Figure 10: Overview of the attenuation fit results for the Test Beam detector calibration simulation. Each cell represents the result of the attenuation fit to the energy response in the centre of that cell. The blank cells are uncalibrated.

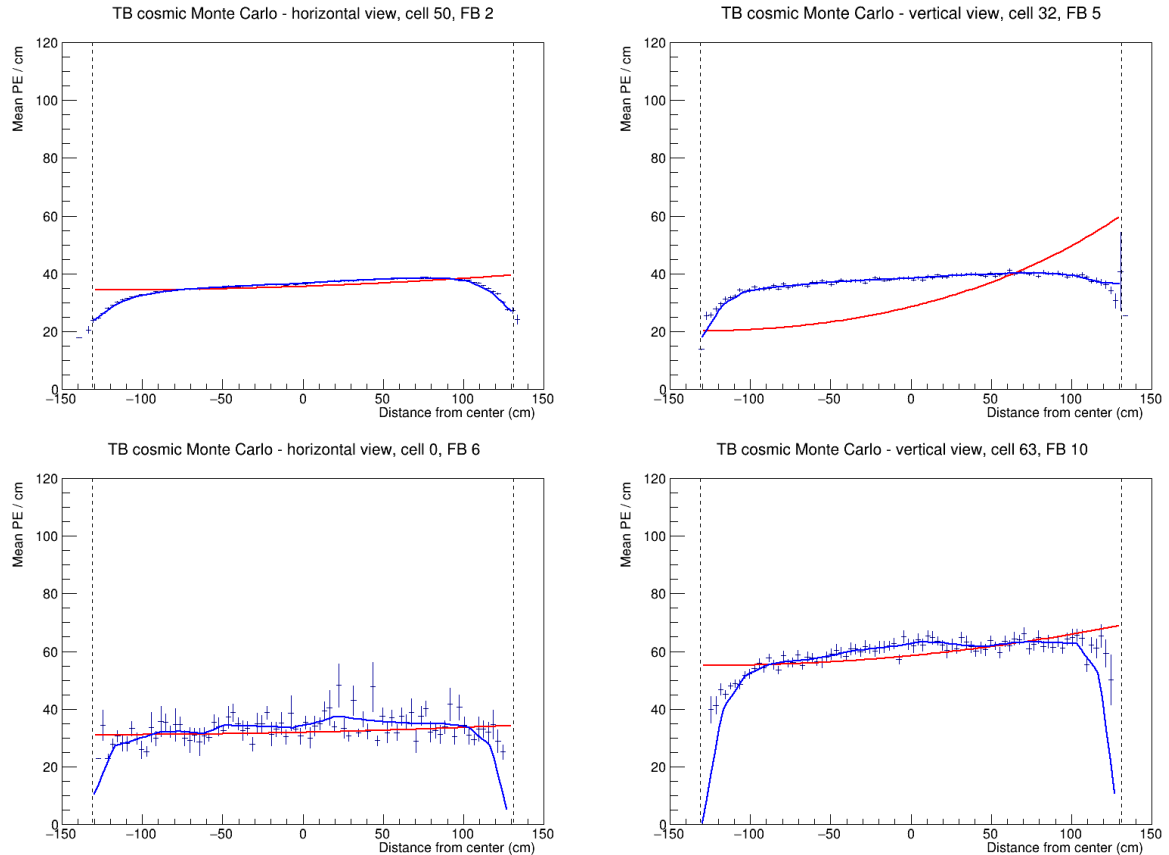
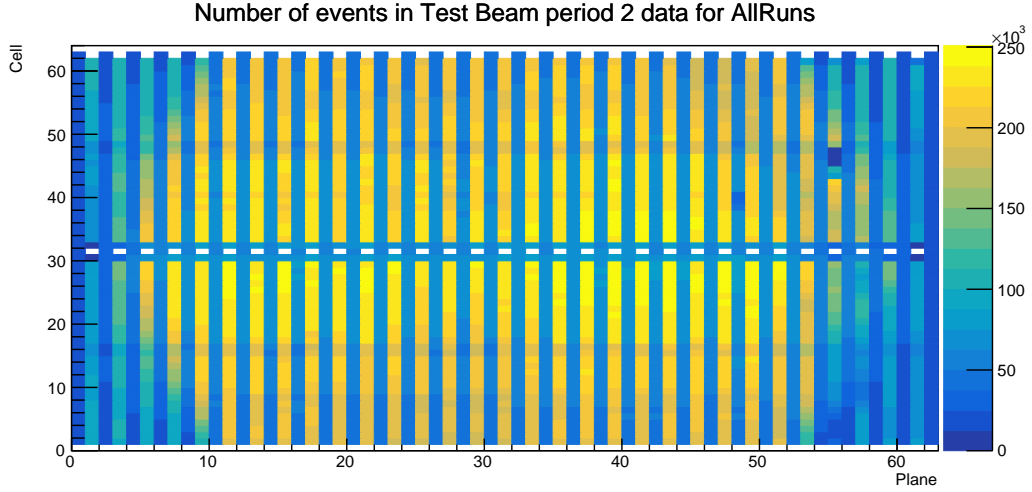


Figure 11: Attenuation fits for a selection of cells in the Test Beam calibration simulation. Top left is an example of a successful attenuation fit, top right is a failed fit due to statistical fluctuation in the last bin and the bottom plots show failed fits for cells on the edges of the detector.

## 349 4.4 Period 2 data

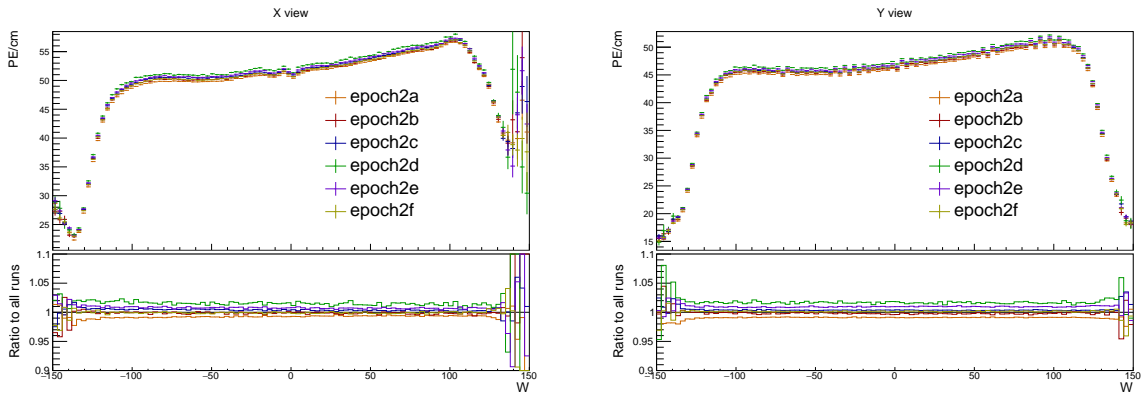
350 The issue with underfilled cells described in section 2 was present throughout the period 2 data  
 351 taking. This can be clearly seen on figure 12, represented by the empty cells 31 and 63 in the  
 352 horizontal planes, which were marked as bad channels and therefore ignored during production  
 353 of calibration samples. This also affects the neighbouring cells to the underfilled cells, which  
 354 have fewer events due to the tricell condition (see section 3).



355 Figure 12: Distribution of events in the period 2 Test Beam data calibration sample.

356 There was also an issue of likely switched cables from the readout in plane 55 between cells  
 357 3 and 46 [29], which can also be seen on figure 12 as dark spots. This is manifested as fewer  
 358 total number of events in those cells and in their neighbours, again due to the tricell condition.

359 Officially, period 2 is divided into 6 epochs 2a - 2f, compared on figures 13,14 and 15. The  
 360 epochs mostly differ in the use of various FEB firmwares, with epoch 2c being a trigger study  
 361 with paddles. As can be seen on the plots, the individual epochs vary only slightly, and only in  
 362 a small normalization difference. We decided to calibrate the entire period 2 together, without  
 splitting it into any smaller samples.



363 Figure 13: Uncorrected average energy response as a function of the position within a cell (w)  
 364 for epochs in period 2. It is clear that there is no significant difference between the various  
 365 epochs.

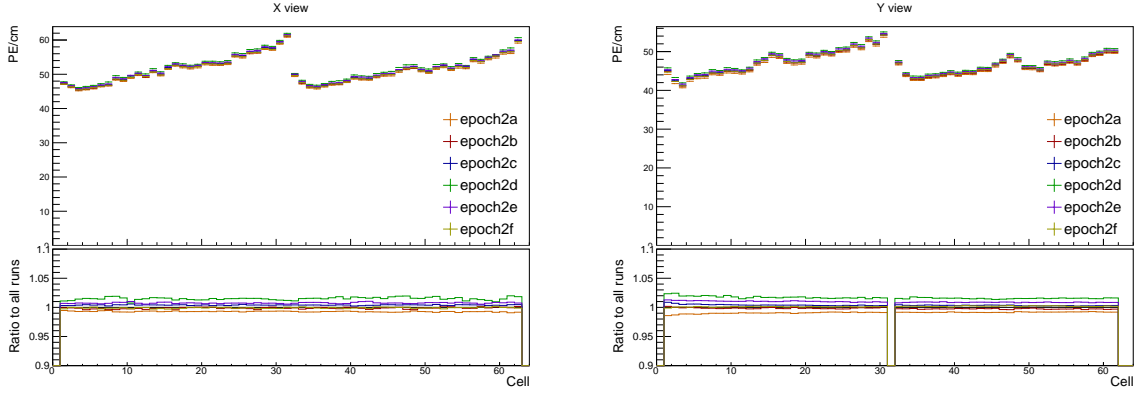


Figure 14: Uncorrected average energy response as a function of cells for epochs in period 2.

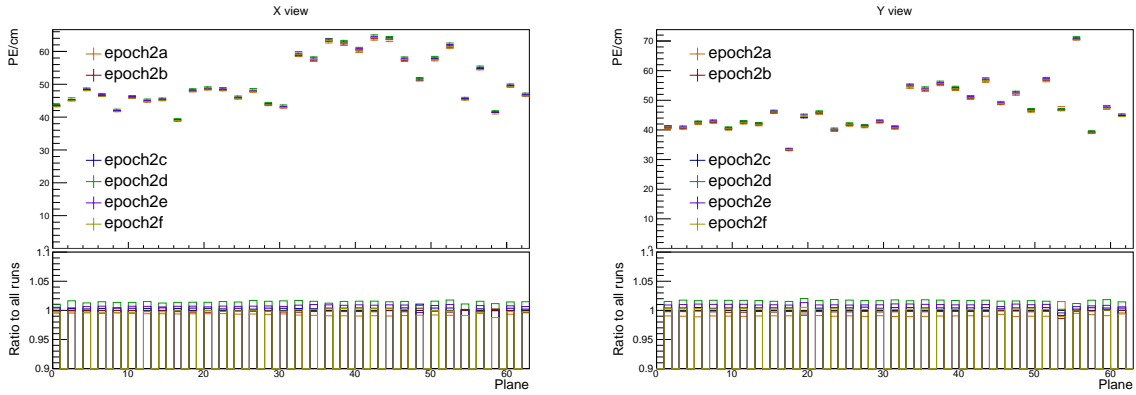


Figure 15: Uncorrected average energy response as a function of planes for epochs in period 2.

### 363 Period 2 relative calibration results

364 The results of the attenuation fit for period 2 are summarised on figure 16, showing the fitted  
365 response at the centre of each cell, or a blank cell if it failed calibration.

366 Most of the cells have an expected response, with steady rise towards the readout and a drop  
367 on the edges, as shown on the left plot of figure 17.

368 Some cells have a non-flat response across the cell, with one or more regions with a drop  
369 in the energy response, as shown on the right plot of figure 17. These low regions are (almost)  
370 certainly a real physical effect caused by zipped, or possibly even twisted fibres [30], present  
371 in all of NOvA's detectors. Relative calibration corrects for this effect in data, but zipped fibres  
372 are not included in simulation, for any of the detectors. This could potentially cause issues with  
373 the ADC threshold in simulation.

374 Since the underfilled cells were marked as bad channels we didn't attempt to calibrate them.  
375 Their neighbours have fewer events due to the tricell condition, but majority of them pass the  
376 calibration condition, as shown on figure 18. The neighbouring cells in plane 1 don't pass  
377 calibration due to low statistics and therefore large fluctuations, as shown on figure 19. This is  
378 likely due to a combination of the tricell condition and plane 1 being on the edge of the detector,  
379 which typically has fewer (accepted) hits than the center, as shown on figure 12.

380 The left half of plane 55 has more than 3 $\times$  larger response than its surrounding planes,  
381 as shown on the left plot of figure 20. Similarly, the left half of plane 57 has slightly lower

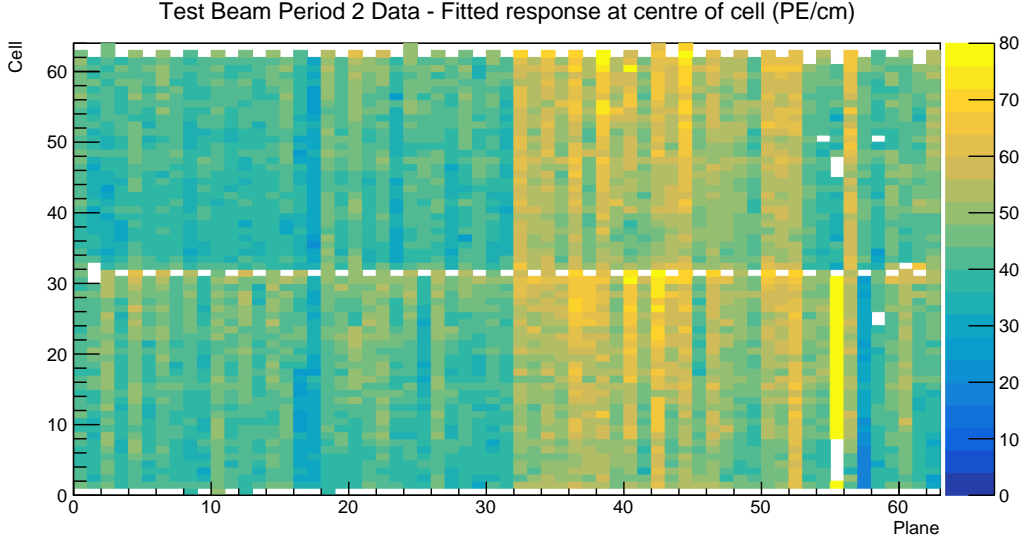


Figure 16: Overview of the relative calibration results for the Test Beam detector period 2 data. Each cell represents the result of the attenuation fit to the energy response in the centre of that cell. The blank cells are uncalibrated.

382 response than the surrounding planes, as shown on the right plot of figure 20. This is due to the  
 383 corresponding APDs/FEBs incorrectly recording different energy response than the real energy  
 384 deposited in the detector. Since this effect is present for all data, not only for the cosmic muons  
 385 used for calibration, it is important to correctly calibrate it out. The issue can arise if these  
 386 FEBs have been "faulty" only for a limited time of the entire calibrated period. Since we are  
 387 doing the attenuation fit on the average response across the whole calibrated period, if an FEB  
 388 records a standard response for half of the time and  $7\times$  larger response for the seconds half,  
 389 calibration is going to assume the response was  $4\times$  larger the entire time, which is incorrect.  
 390 Since both of these planes are in the back of the detector, we decided to ignore this effect for  
 391 period 2.

392 The cells with (probably) swapped cables in plane 55 have almost no events, which affects  
 393 both them and their neighbours as shown of figure 21.

394 Several cells in the end of the Test Beam detector are uncalibrated due to the histogram  
 395 bins on the edges of the cell having an unusually high response, or no events at all, as shown on  
 396 figure 22. It is unknown if this is a real physical effect, possibly related to the fibres, or if it is  
 397 unfiltered noise hits, or something else entirely. Since these cells are in the end of the detector,  
 398 it is fairly safe to ignore them.

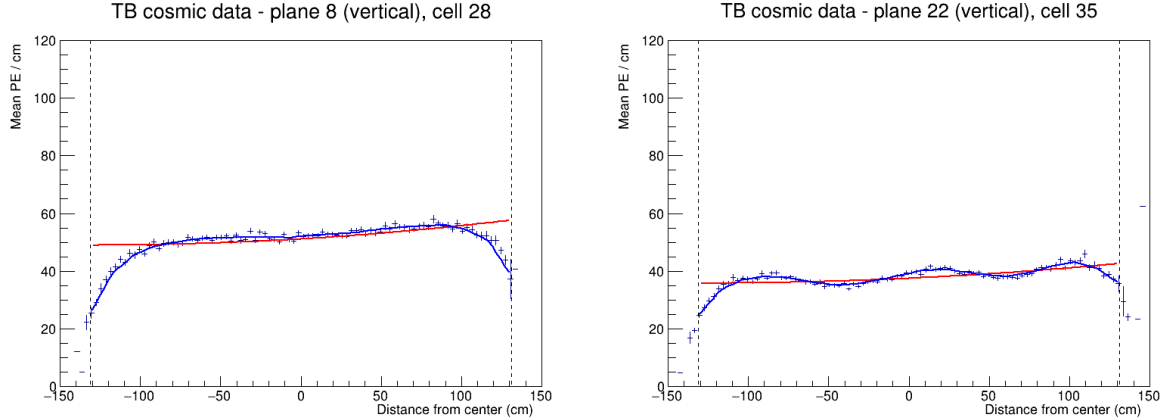


Figure 17: Attenuation fits for a selection of cells in period 2. Left plot shows an example of the standard energy deposition in the Test Beam. Right plot shows the effect of zipped fibres.

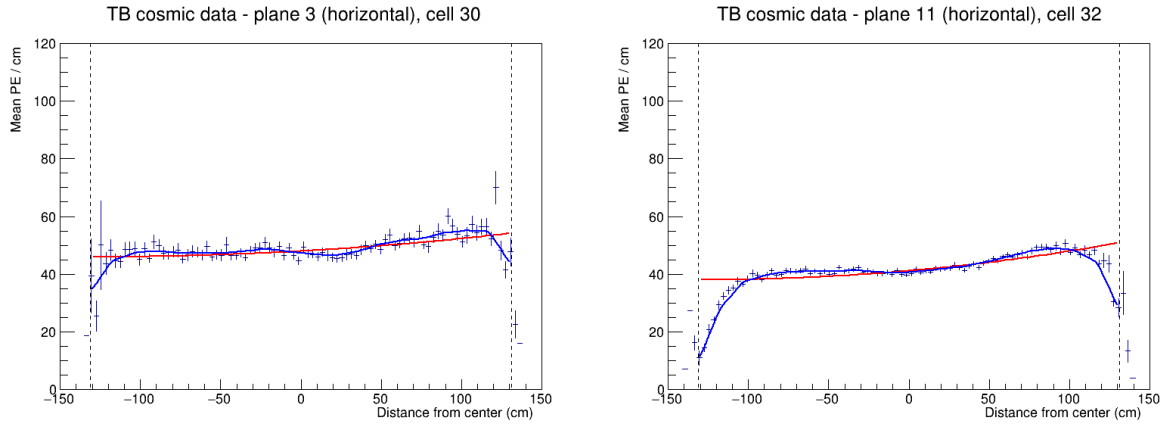


Figure 18: Fit to the energy response in period 2. The cells neighbouring the underfilled cells have fewer events and therefore larger fluctuations than the "usual" Test Beam cell.

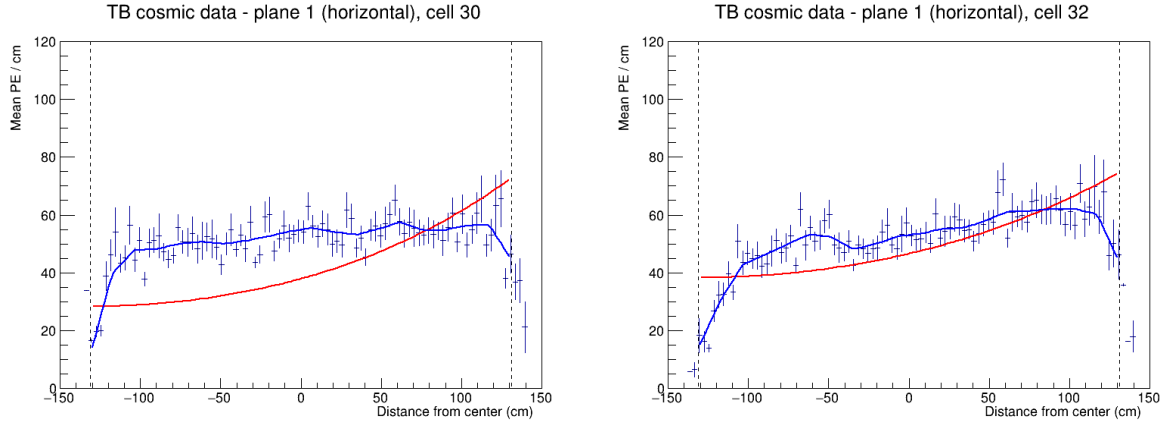


Figure 19: Fit to the energy response in period 2. The neighbouring cells to the underfilled cells in plane 1 are uncalibrated due to low statistics.

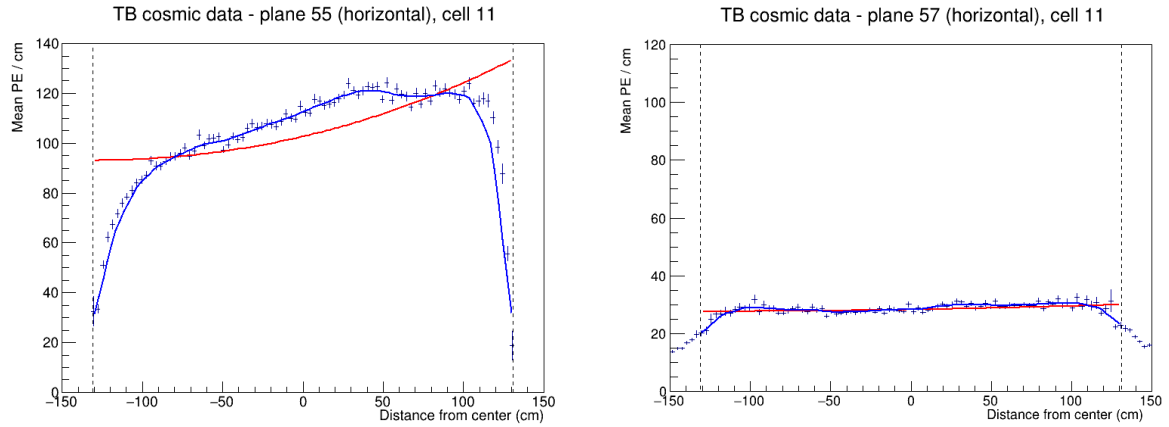


Figure 20: Fit to the energy response in period 2. Lower halves of planes 55 and 57 have a different scale of energy response than the surrounding planes.

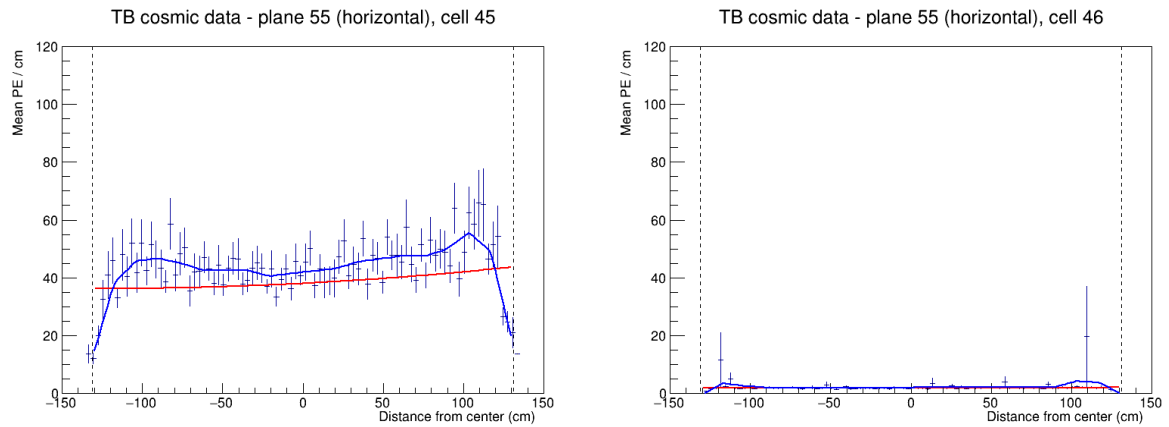


Figure 21: Fit to the energy response in period 2. Cells with swapped readout cables have almost no recorded events as shown on the right plot. This also affect their neighbouring cells due to the tricell condition as shown on the left plot.

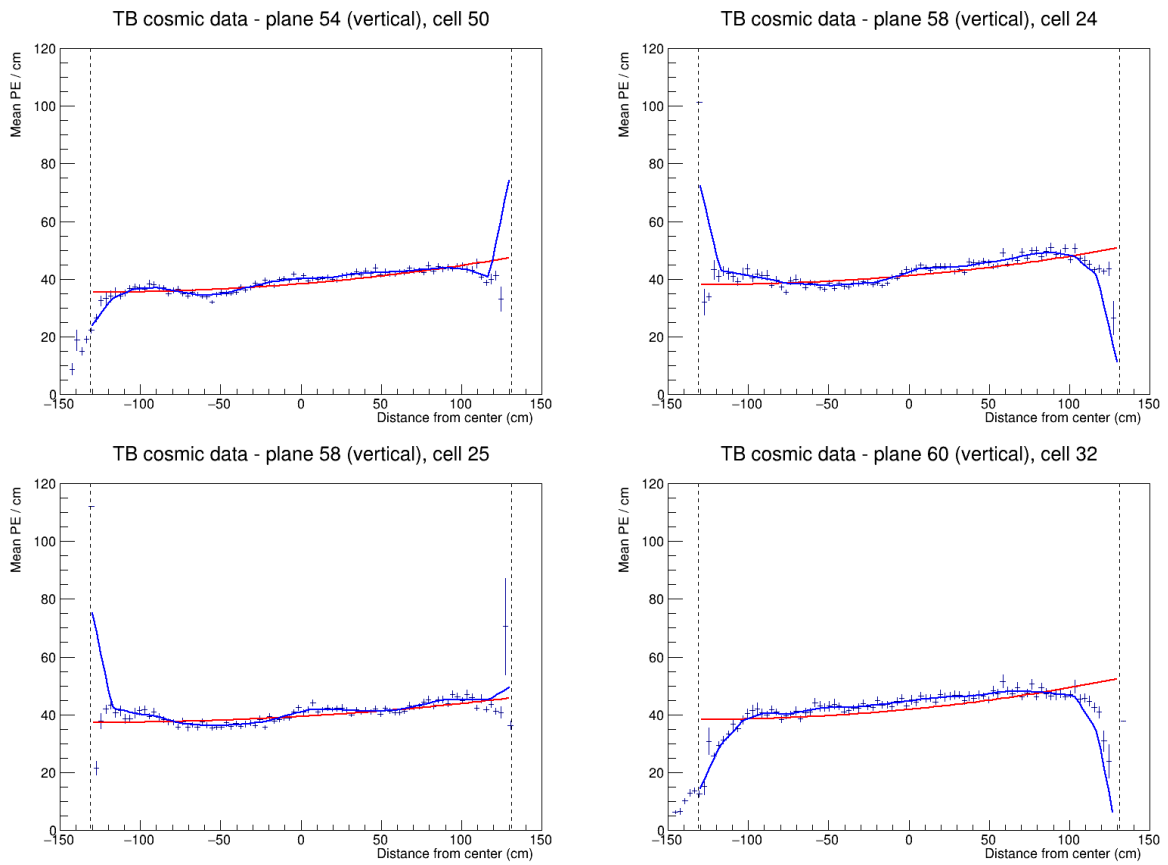


Figure 22: Fit to the energy response in period 2. Examples of cells that have an unusually high or low energy response at the edge of the cell. These cells are not calibrated.

399 **4.5 Period 3 data**

400 The underfilled cells were refilled (or overfilled) during the period 3 data taking. This was the  
401 main motivation for dividing period 3 into individual epochs as shown on table 4. One more  
402 major event that could impact the Test Beam data is the replacement of several faulty FEBs,  
403 which motivated the creation of epoch 3e.

Name	Start date	Reason for creating the epoch
Epoch 3a	January 12 <sup>th</sup> 2021	Underfilled cells
Epoch 3b	April 21 <sup>st</sup> 2021	Overfilling the back 9 horizontal planes and the 7th horizontal plane from the front
Epoch 3c	April 27 <sup>th</sup> 2021	Overfilling of the 15 front horizontal planes (except the 7th, which was already done) and the 14th horizontal plane
Epoch 3d	April 30 <sup>th</sup> 2021	Overfilling of the remaining 8 horizontal planes
Epoch 3e	May 12 <sup>th</sup> 2021	FEB swaps

Table 4: Test Beam period 3 epochs, their start dates and the reason for their separation.

404 The refilling of the underfilled cells can be clearly seen on the cell hits distribution on figure  
405 23 and on the distribution of energy deposition across horizontal cells (Y view) on figure 25.

406 From the cell hits distributions we can also see there are a few channels (cells) that were  
407 likely dead for a certain time and weren't recording the same number of events as the surrounding  
408 cells. This is specifically plane 48, cell 39 in all of period 3 and plane 18, cell 31 in epochs  
409 3d and 3e.

410 The energy distributions across cells and planes in the X view (vertical) on figures 25 and 26  
411 shows, that the top half of plane 58 has a very distinctly different energy deposition compared  
412 to the rest of the cells. However figure 23 shows that this part has the same number of events.  
413 This is the FEB, that has the largest impact on the calibration (and overall) out of the faulty  
414 FEBs replaced before the start of epoch 3e.

415 From these considerations, we decided to calibrate epochs 3a, 3b and 3c together (all epochs  
416 containing any underfilled cells) and to separately calibrate epochs 3d and 3e. The faulty FEB  
417 in the top of plane 58 is far enough in the back of the detector, that we didn't find it necessary  
418 to calibrate epochs 3d and 3e separately. Also epochs 3b and 3c only contain a few days worth  
419 of data, which wouldn't be enough for a successful attenuation fit.

420 **Combined epochs 3a, 3b and 3c relative calibration results**

421 The results of the attenuation fit are summarised on figure 27 showing cell × plane distribution  
422 of the fitted response at the centre of each cell.

423 We can see that some of the underfilled cells that have been refilled for epochs 3b or 3c  
424 are now calibrated thanks to including these two short epochs into the same attenuation fit. An  
425 example of energy deposition in such a cell is on the left plot of figure 28.

426 Same as in period 2, most of the neighbouring cells to the underfilled cells are calibrated,  
427 except for cell 32 in plane 1, shown on the right of figure 28. This is due to the low statistics at

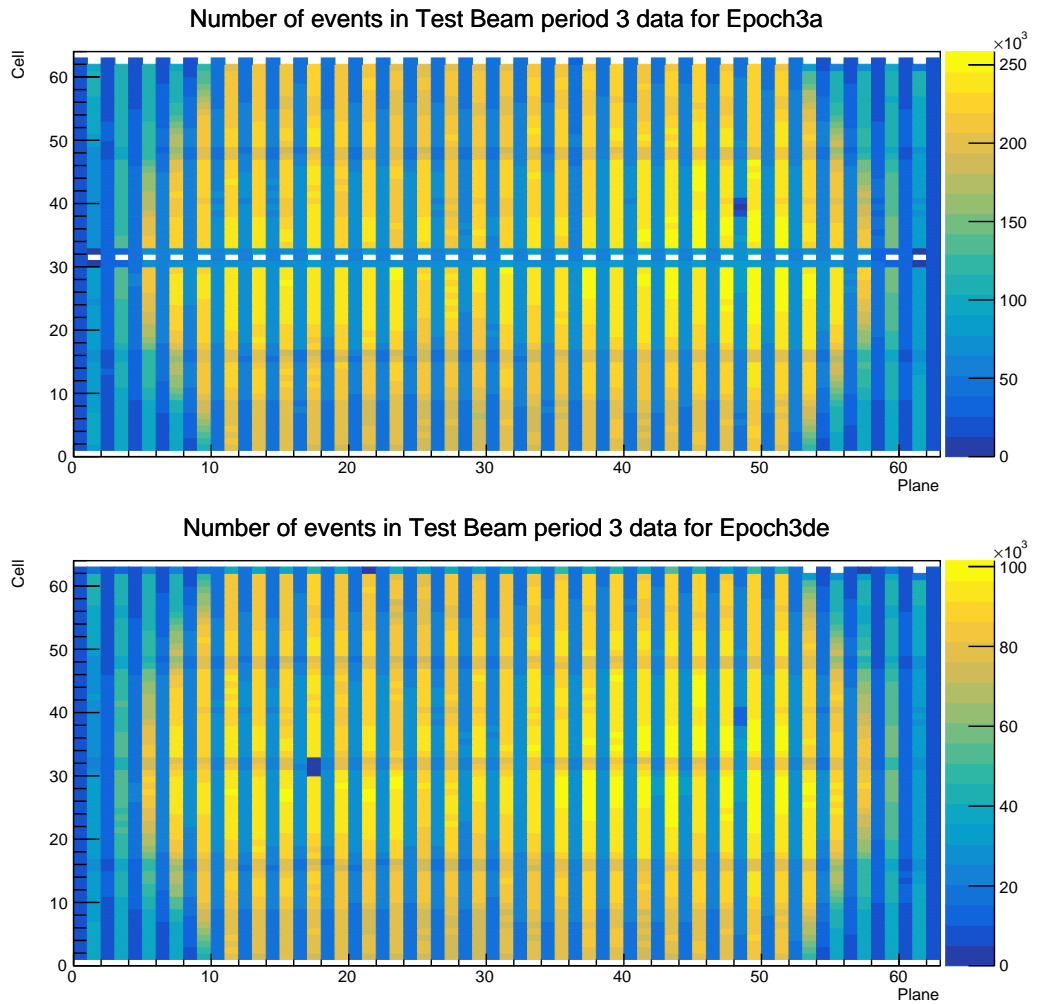


Figure 23: Distribution of events in the period 3 Test Beam data calibration sample. Comparison of Epoch 3a data before the refilling of the underfilled cells and Epoch 3de (combination of Epochs 3d and 3e) after the full refilling.

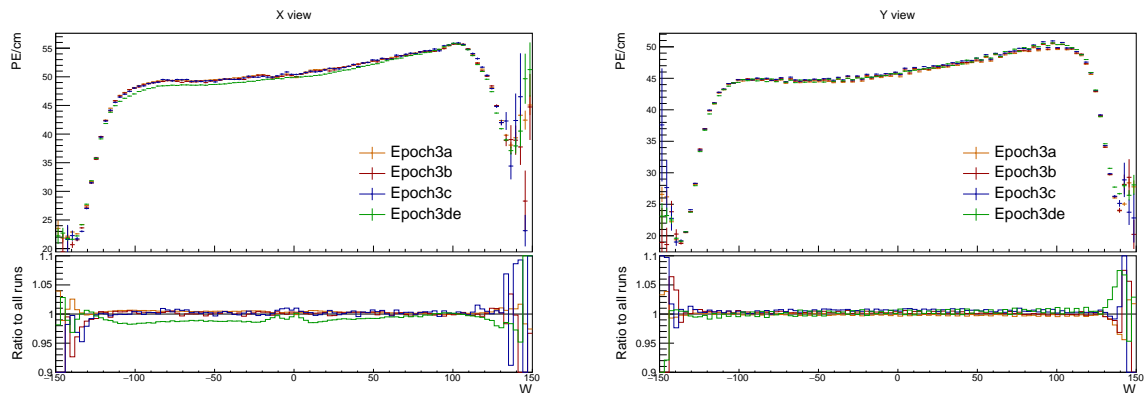


Figure 24: Uncorrected average energy response as a function of the position within a cell ( $w$ ) for epochs in period 3.

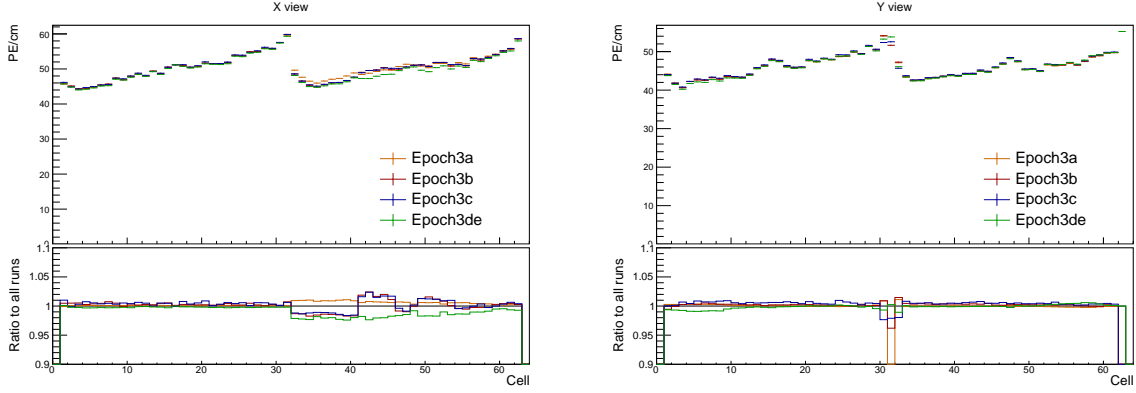


Figure 25: Uncorrected average energy response as a function of cells for epochs in period 3.

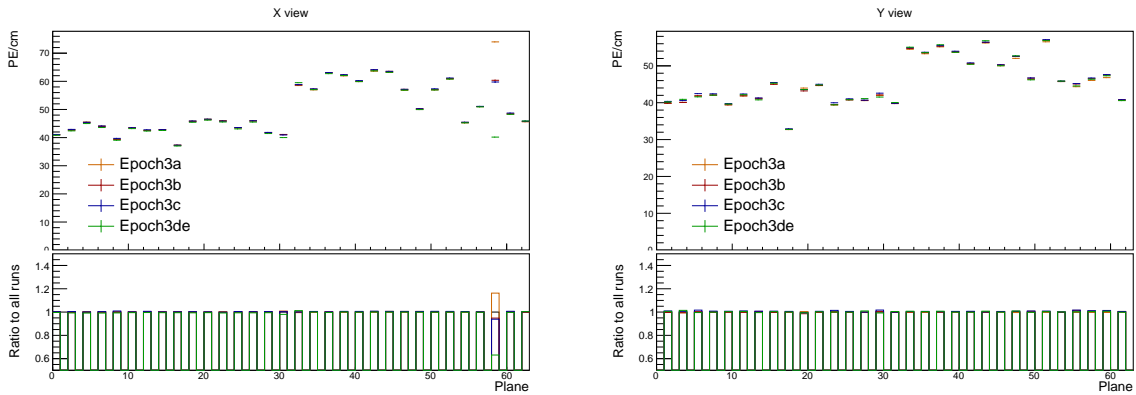


Figure 26: Uncorrected average energy response as a function of planes for epochs in period 3.

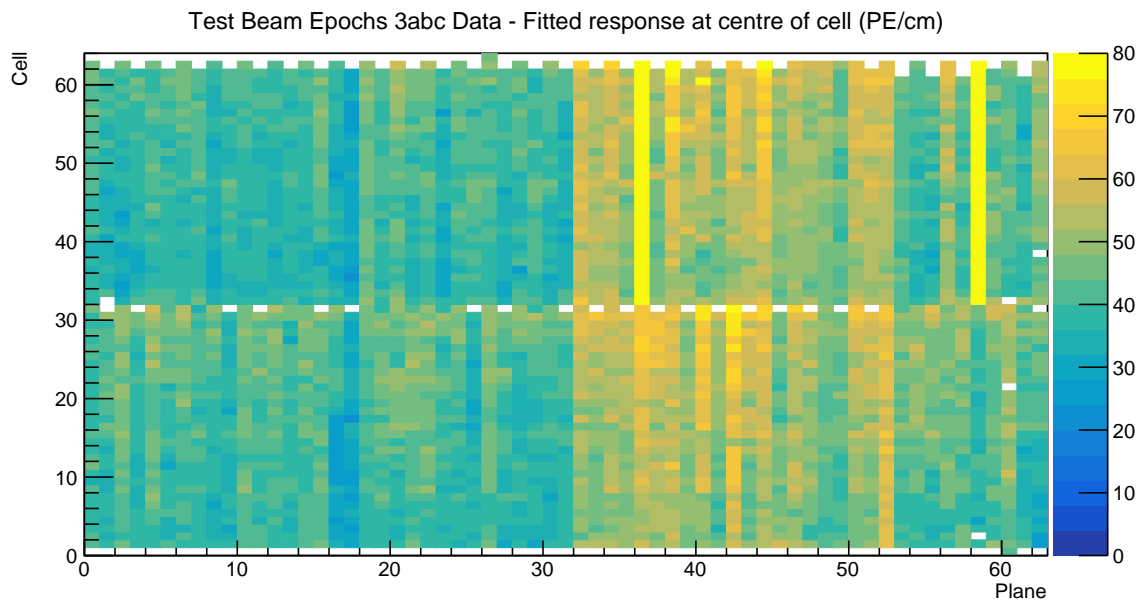


Figure 27: Overview of the relative calibration results for the Test Beam detector period 3, combined epochs 3a, 3b and 3c data. Each cell represents the result of the attenuation fit to the energy response in the centre of that cell. The blank cells are uncalibrated.

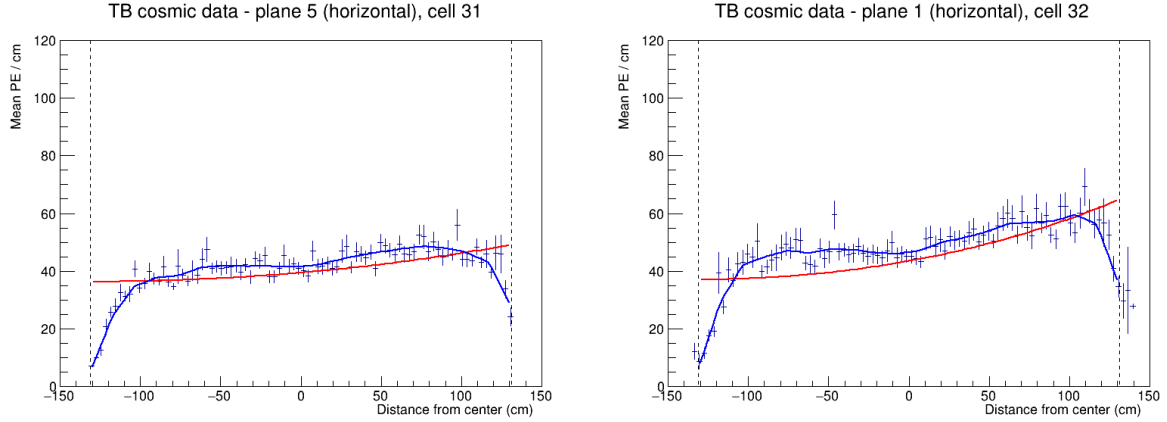


Figure 28: Fit to the energy response in epochs 3 a, b and c. Some underfilled cells that have been refilled in epochs 3b and 3c are now calibrated as shown on the left plot. Cell 32 in plane 1 is the only neighbouring cell to the underfilled cell that didn't manage to get calibrated due to low number of events.

428 the edges of the detector.

429 There is a couple of notably faulty FEBs with a different energy response than their neig-  
430 bours. Besides the expected top half of plane 58, which has about  $5\times$  larger response than the  
431 usual, it's also the top half of plane 36, which has about  $2.5\times$  larger response as its neighbours.  
432 This could mean that the FEB in plane 36 was faulty only for a limited time compared to the  
433 FEB in plane 58. The energy deposition for these cells is shown on figure 29.

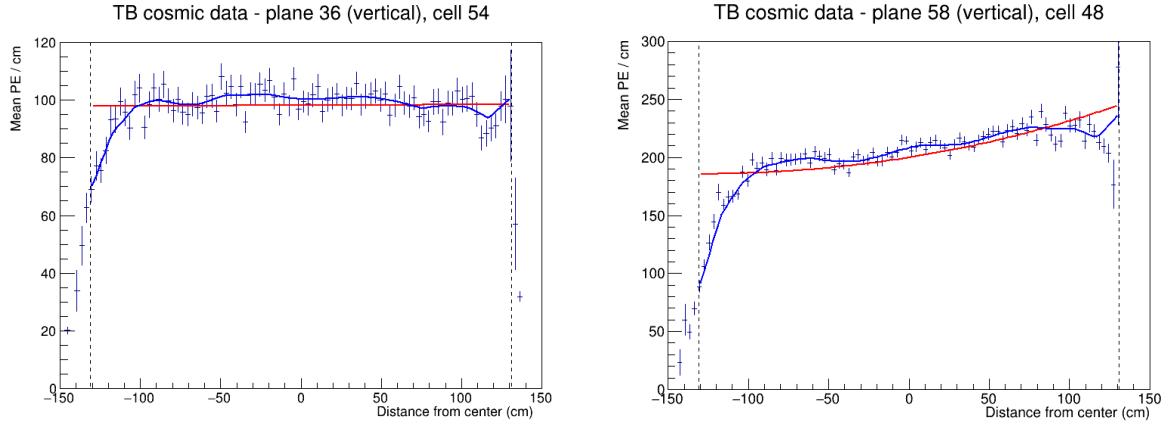


Figure 29: Fit to the energy response in epochs 3a, 3b and 3c. The most obvious faulty FEBs that have a significantly larger energy response than their neighbours.

434 Similarly as in period 2, there are a few cell in the back of the detector that have a sharp  
435 rise in the energy response at the edge of the cell, which causes them to be uncalibrated. This  
436 can be seen on figure 30.

#### 437 Combined epochs 3d and 3e relative calibration results

438 The results of the attenuation fits for epochs 3d and 3e are shown on figure 31. There we can  
439 see the expected uncalibrated cells in plane 17 related to the dead channel (or possible still

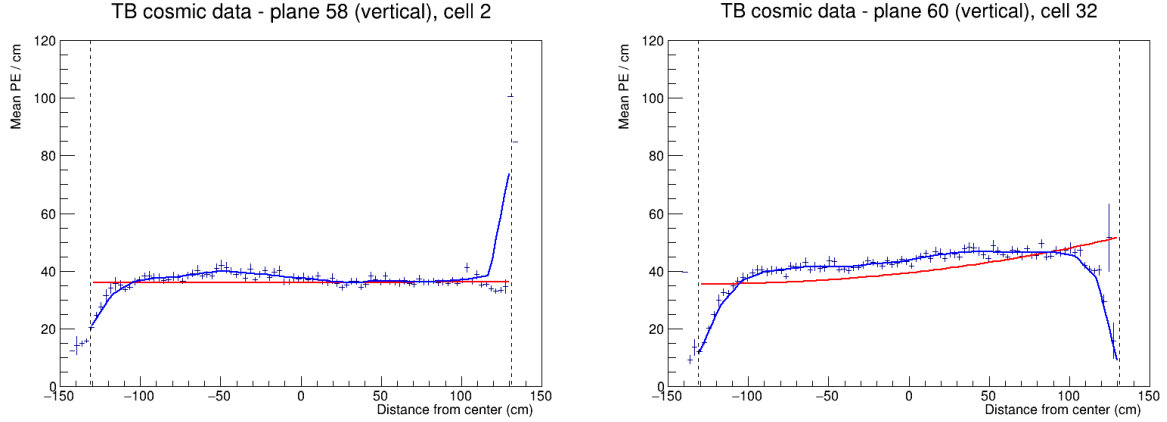


Figure 30: Fit to the energy response in epochs 3a, 3b and 3c. Some cells are not calibrated due to large fluctuations at one edge of the cells.

<sup>440</sup> underfilled cell). The energy deposition for this cell and one of its neighbours is shown on  
<sup>441</sup> figure 32.

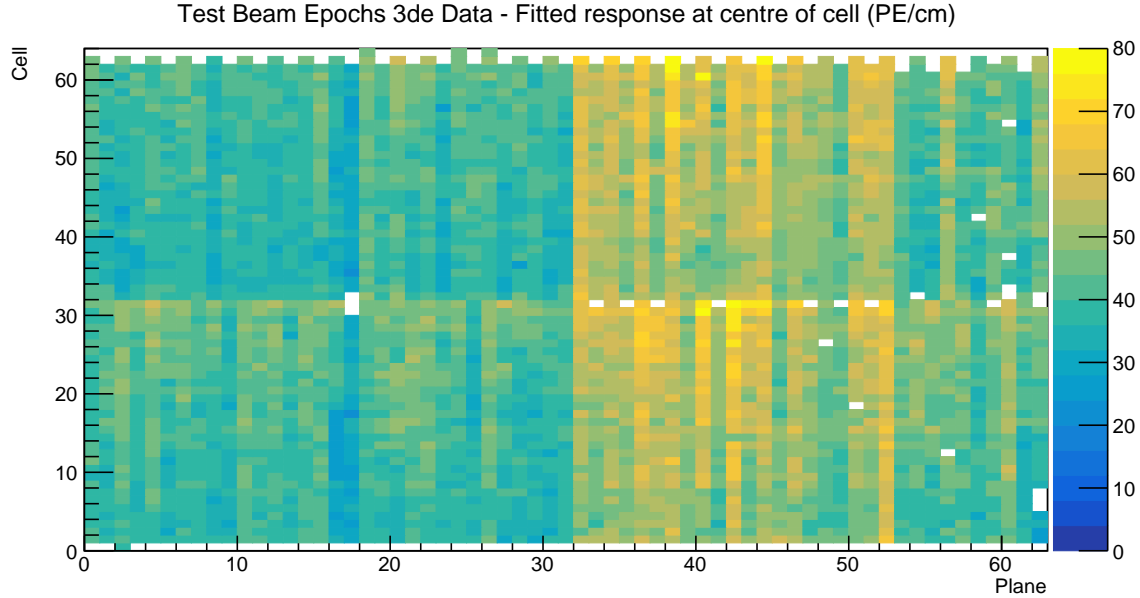


Figure 31: Overview of the relative calibration results for the Test Beam detector period 3, combined epochs 3d and 3e data. Each cell represents the result of the attenuation fit to the energy response in the centre of that cell. The blank cells are uncalibrated.

<sup>442</sup> Epochs 3d and 3e should have all the previously underfilled cells now refilled, but as can  
<sup>443</sup> be seen on figure 31, there's several of these cells that are still (officially) uncalibrated. The  
<sup>444</sup> energy deposition in these cells is shown on figure 33. Here we can see that these cells have  
<sup>445</sup> a fairly large discrepancy between the left and right side of the cells. This is caused by using  
<sup>446</sup> different scintillator oils for the initial filling of the cells and for the refilling. Specifically, these  
<sup>447</sup> cells have been initially filled with the Ash River and the Texas oils, which have higher energy  
<sup>448</sup> depositions compared to the NDOS oil that was used for the refilling during period 3. These

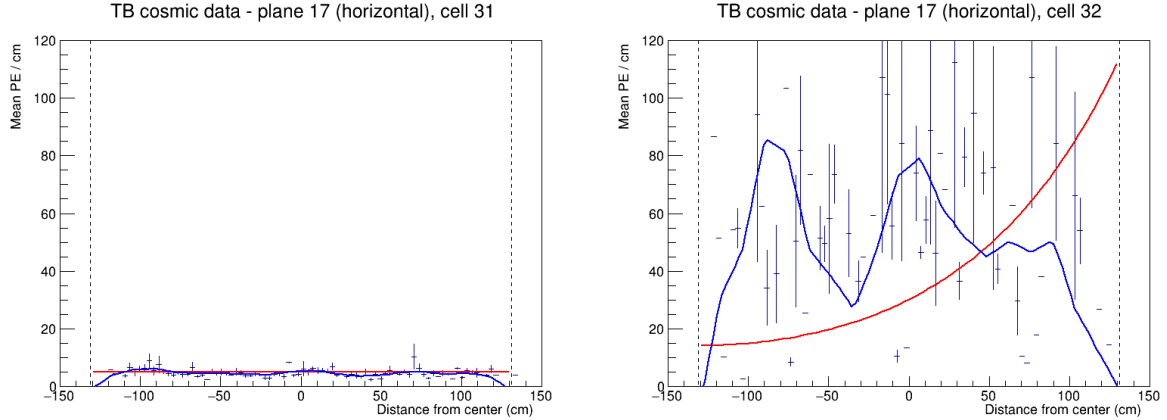


Figure 32: Fit to the energy response in epochs 3d and 3e. Possibly dead channel or still underfilled cell.

449 oils clearly didn't mix properly which causes a different energy deposition in different parts  
 450 of the cells. This is a physical effect that should be accounted for in the calibration and as  
 451 we can see, the attenuation fits are actually performing reasonably well. The large  $\chi^2$  value is  
 452 most likely caused only by the unusual shape of the distribution, which the fit is not build for.  
 453 **We have therefore decided to manually change the  $\chi^2$  inside the cvs tables (results of the**  
 454 **attenuation fits), so that the  $\chi^2 < 0.2$  and these cells are officially considered calibrated.**

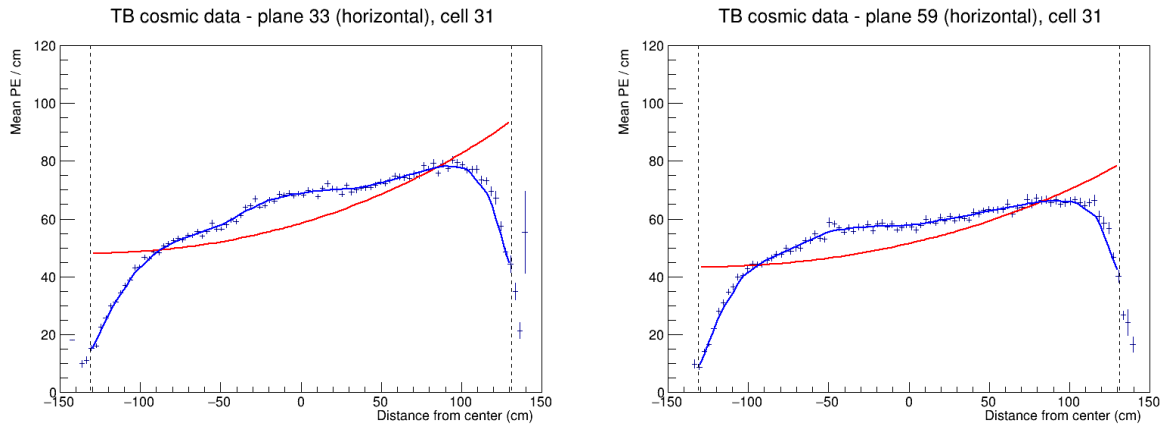


Figure 33: Fit to the energy response in epochs 3 d and e. The scintillator oil used for refilling of the underfilled cells has lower energy response than the oil used for the initial filling. These oils didn't mix properly causing a different energy response in the left and right side of the cell.

455 Some of the cells in the back of the detector have a rise, or drop in energy deposition at the  
 456 edge of the cell, as can be seen on figure 34. This is similar to the effect seen in period 2 and  
 457 epochs 3a+3b+3c and since it's again concentrated in the end of the detector, we ignored these  
 458 cells and left them uncalibrated.

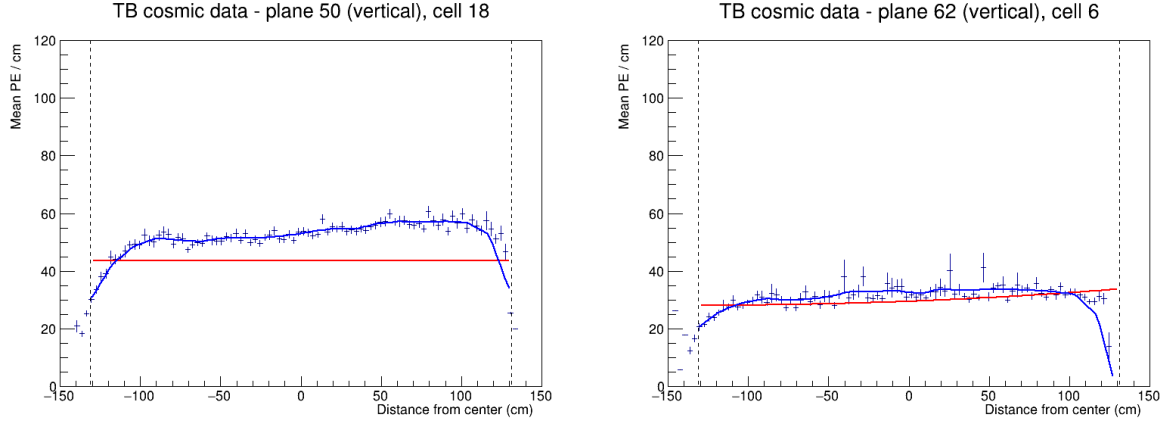


Figure 34: Fit to the energy response in epochs 3d and 3e. Some cells have a drop, or a rise of energy response at the edge of the cell. This can be caused by low statistics.

## 459 4.6 Period 4 data

460 The period 4 Test Beam data taking period is the best data we managed to collect with almost  
 461 an ideal detector conditions. There's only a few commissioning runs in the very beginning of  
 462 period 4, which uncovered some dead channels or faulty FEBs that were immediately fixed.  
 463 These runs make up epoch 4a, shown on the top plot of figure 35. There is also a few runs  
 464 during which we masked parts of the detector to help with FEB saturation [31], which can  
 465 clearly be seen on the middle plot of figure 35.

466 Figures 36, 37 and 38 show that the epoch 4a and the cell masking study did have a notice-  
 467 able impact on the energy deposition across the detector. We have therefore decided to ignore  
 468 these runs and only calibrate the rest of the period 4 data.

### 469 Period 4 relative calibration results

470 Results of the attenuation fits for period 4 are summarised on figure 39. We can see that  
 471 majority of the detector is calibrated, besides some cells on the edge of the detector, a few  
 472 formerly underfilled cells (left plot on figure 40), and one cell with an unusually high response  
 473 at the edge of the cell (right plot on figure 40).

474 We treated the formerly underfilled cells the same way as in epochs 3d and 3e, by man-  
 475 ually changing their  $\chi^2$  inside the csv files to be  $< 0.2$  and therefore making them officially  
 476 calibrated.

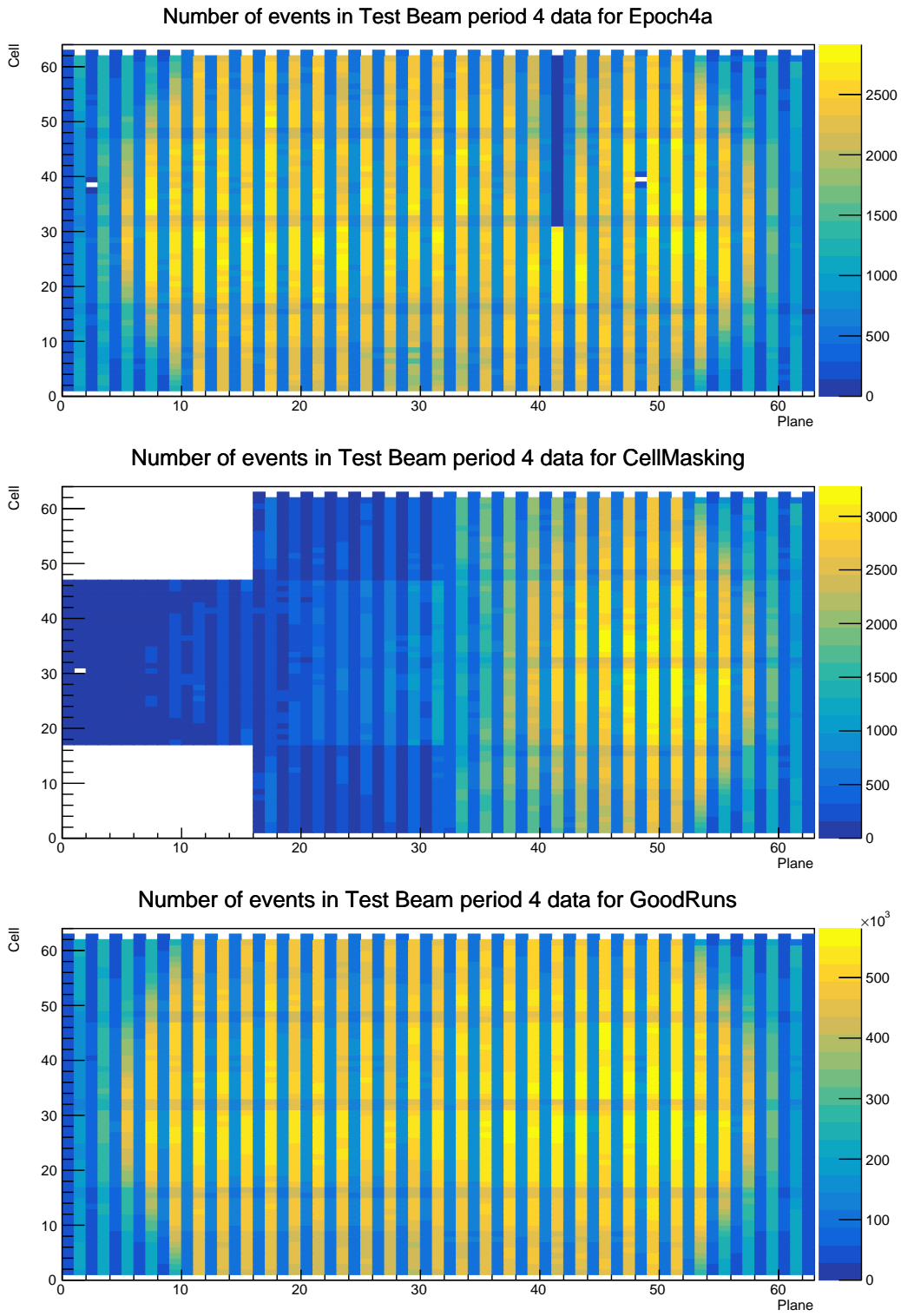


Figure 35: Distribution of events in the Test Beam period 4 data calibration sample. The top plot shows the first three commissioning runs, the middle plot the status of the detector during the Cell Masking studies and the bottom plot shows the rest.

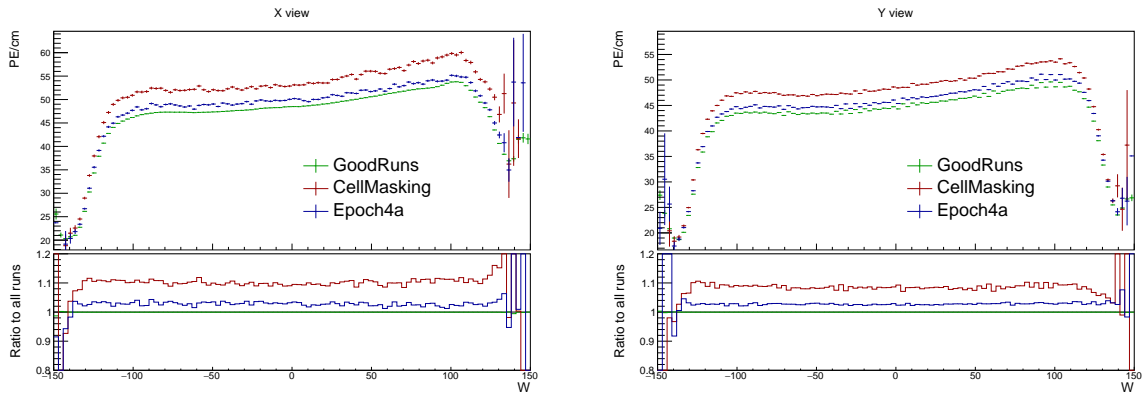


Figure 36: Uncorrected average energy response as a function of the position within a cell ( $w$ ) for epochs in period 4.

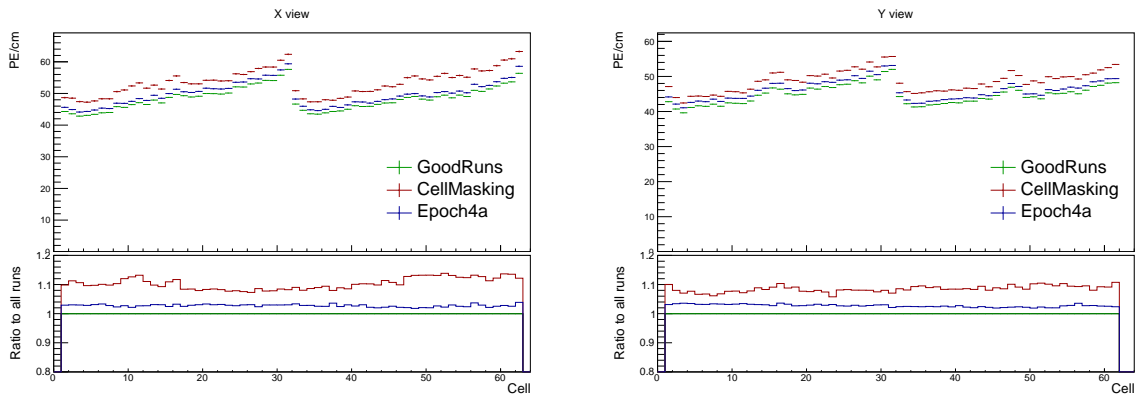


Figure 37: Uncorrected average energy response as a function of cells for epochs in period 4.

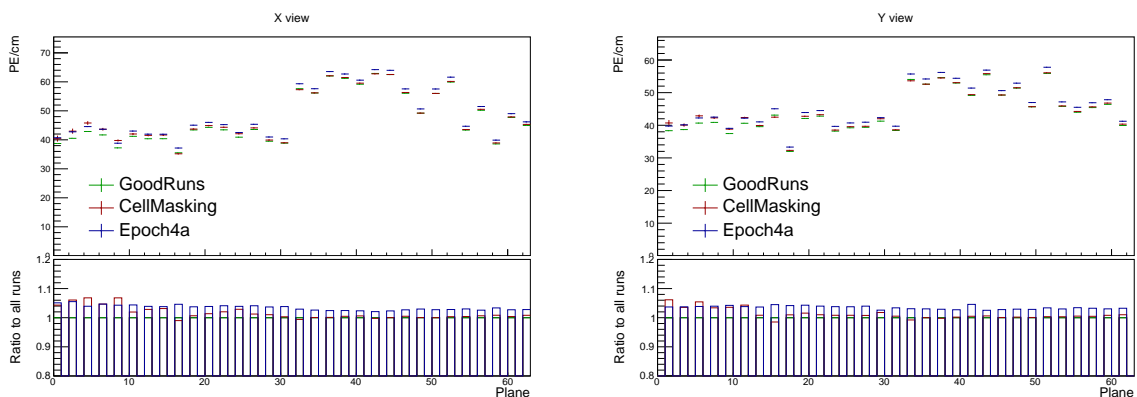


Figure 38: Uncorrected average energy response as a function of planes for epochs in period 4.

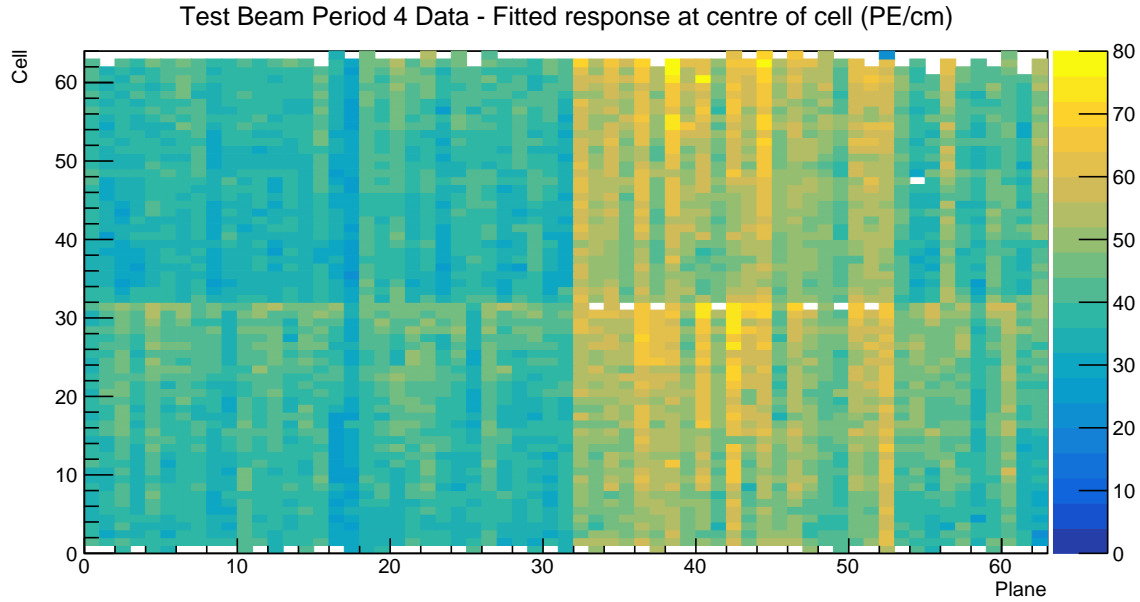


Figure 39: Overview of the relative calibration results for the Test Beam detector period 4 data. Each cell represents the result of the attenuation fit to the energy response in the centre of that cell. The blank cells are uncalibrated.

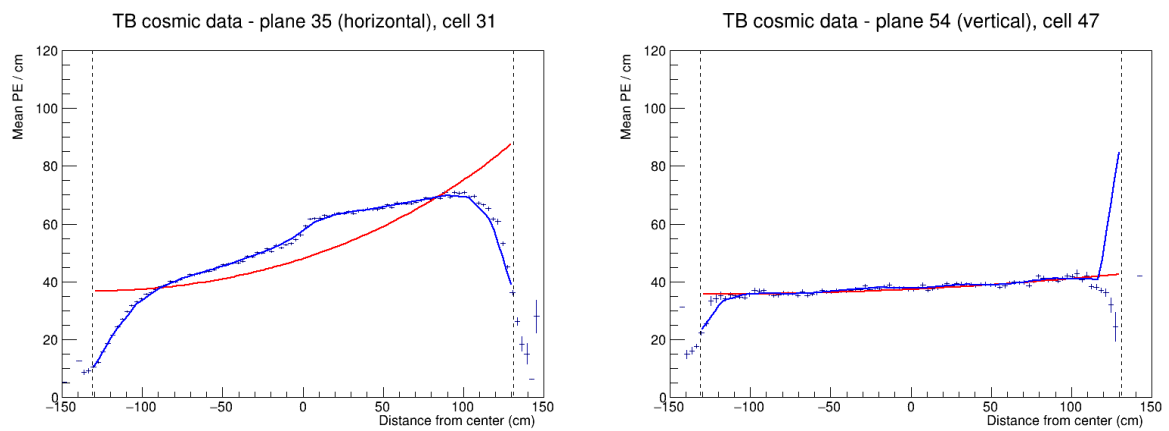


Figure 40: Fit to the energy response in period 4. Previously underfilled cells refilled with a scintillator of a different quality causing an unusual distribution of energy deposition (left). Unusually high energy response at the edge of the cell 47 (right).

## 4.7 Absolute calibration results

To get the absolute energy scale we look at the stopping muon sample, apply the relative calibration results and the absolute calibration cuts to select only well-understood minimum ionising muons. The absolute calibration cuts are mostly the same as for the other detectors (hits 1-2 m from the end of track, pathlength > 0,  $PE > 0$ ,  $PECorr > 0$ ,  $PECorr/cm < 100$ ), but with a smaller cell window  $-80 < w < 80$  cm to remove hits at the cell edges.

We then look at the distributions of the reconstructed energy response in units of  $PECorr/cm$  (for all data and simulation samples), and true energy response in units of  $MeV/cm$  (only for simulation) in each view, as shown on figure 41. The mean of these distributions is the  $MEU_{View,Reco/True}$  value, with an uncertainty calculated as  $StdDev/\sqrt{N_{Entries}}$  from the distribution. The MEU for each sample and view is shown on table 5.

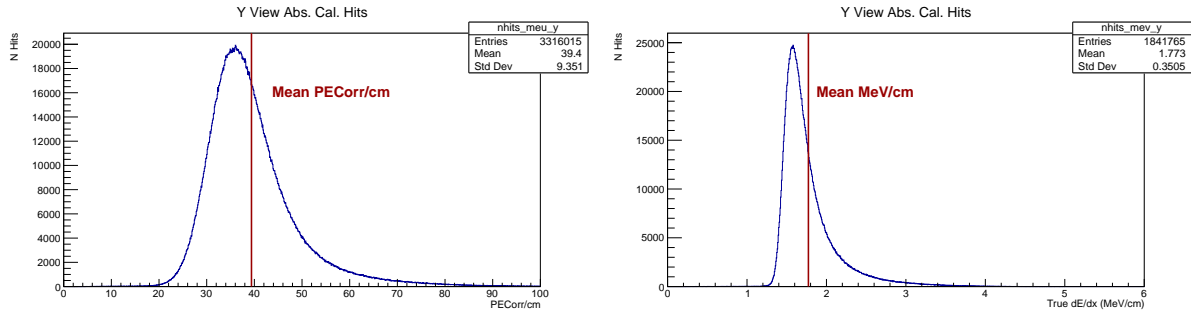


Figure 41: Example distributions of reconstructed (left) and true (right) energy response of stopping muons 1-2 m from the end of their tracks. The mean of the reconstructed (true) response is the reconstructed (true) MEU unit.

Sample		X view		Y view		Combined	
		NHits	MEU	NHits	MEU	MEU <sub>Reco</sub>	MEU <sub>Reco</sub> Err
Data	Period 2	2.322e+05	38.7	1.413e+06	39.4	39.05	0.007
	Epochs 3abc	2.638e+05	38.49	1.621e+06	39.4	38.94	0.007
	Epochs 3de	1.049e+05	38.63	6.725e+05	39.42	39.02	0.01
	Period 4	5.268e+05	38.63	3.316e+06	39.4	39.01	0.005
	Simulation	2.829e+05	40.17	1.842e+06	39.93	40.05	0.006

$$MEU_{True} = 1.772 \text{ MeV/cm} \quad MEU_{True} \text{ Err} = 0.0002 \text{ MeV/cm}$$

Table 5: Table of the absolute calibration results.  $MEU_{Reco}$  values (top table) are in units of  $PECorr/cm$  and  $MEU_{True}$  values (bottom table) are in units of  $MeV/cm$

We don't apply the absolute energy scale separately for each view, instead we combine the two views into a single  $MEU_{Reco}$ , or  $MEU_{True}$  value. To combine the MEU value we take a simple average  $(MEU_X + MEU_Y)/2$ , without accounting for the different statistics of the two views. To get the uncertainty on the final value, we calculate it as  $1/\sigma_{Combined}^2 = 1/\sigma_X^2 + 1/\sigma_Y^2$ . This uncertainty is however **not** the uncertainty used in NOvA for the absolute energy scale. Instead, we use a data-simulation comparison of special samples to derive an uncertainty on the absolute energy scale [32]. The final combined values are highlighted in table 5. Here  $MEU_{Reco}$  values are all in units of  $PECorr/cm$ .

496 For each calibrated sample we write the combined  $MEU_{Reco}$  value into an `calib_abs_consts.csv`  
497 file, together with its uncertainty and with the  $MEU_{True}$  value, which is common for all samples.

## 498 4.8 Results

499 The results of the relative and the absolute calibration, in form of the csv files, are stored in  
500 `/grid/fermiapp/products/nova/externals/calibcsvs/` and are applied within NOvA-  
501 Soft in the calibration tag v15.09 and higher.

502 The csv files follow the official NOvA calibration naming convention, which is  
503 `calib_{abs/atten}_{consts/points}.{nd/fd/tb}.{data/mc}.{version}.{period}.csv`.  
504 Here version is the calibration tag (i.e. v15) and period is the range of runs for that sample  
505 (i.e. r100857-r101356 for the combined epochs 3a, 3b, and 3c, or r-r for simulation, since it  
506 is not divided into different periods).

507 To create the calibration tag we've asked Lisa Koerner for help. Lisa is a NOvA calibration  
508 expert who wrote the instructions for calibration tagging [33]. It is possible to do it ourselves  
509 following these instructions, but it is advised to consult the detector systematics group before  
510 hand.

511 We have also stored the final calibration results in a special location created for safekeep-  
512 ing of Test Beam calibration files: `/nova/ana/testbeam/calibration`. Here we have also  
513 copied all of the attenuation profiles used in the relative calibration. These can be very useful  
514 in case someone wants to re-do the calibration, as it allows to skip the prestaging of the calibra-  
515 tion plist samples (the pliststop samples are much smaller and therefore easier to prestage).  
516 If there has been no change to the calibration samples, it is possible to skip the creation of  
517 attenuation profiles and reuse the existing files.

## 518 4.9 Validation

519 To validate the results of the Test Beam calibration we look at the stopping muon sample used  
520 for the absolute calibration, since these events have the most consistent and reliable energy  
521 deposition.

522 In plots on figures 42-55 we look at distributions of variables used during the calibration,  
523 namely  $PE$ ,  $PECorr$ ,  $Pathlength$ ,  $PE/cm$  and  $PECorr/cm$ . Their distributions are over a range  
524 of variables we tried to correct the energy deposition in, namely position within a cell  $w$ , cell  
525 number, plane number, track angles and time.

526 The most important validation plots are the distributions of  $PECorr/cm$ , which should be  
527 completely flat. This would mean that all the deposited energy results in an equivalent recorded  
528 energy wherever and whenever in the Test Beam detector it occurred. As can be seen on the  
529 validation plots, this was successfully achieved and the  $PECorr/cm$  distributions are mostly  
530 flat across all studied variables.

531 The distribution of  $PECorr/cm$  across cells in X view on figure 46 seems fairly scattered,  
532 however this is mostly due to the better resolution of this plot and the dispersion of the energy  
533 deposition across cells isn't large enough to constitute further investigation.

534 The distributions of  $PECorr/cm$  across planes in the X view (figure 46) shows a notice-  
535 able smaller corrected energy response of stopping muons in plane 36. This means that the  
536 relative calibration over-corrected the energy response due to the through-going muons having  
537 unusually high energy response (as shown on figure 29), but not the selected stopping muons.

538 The most likely cause is that the impacted FEB was "faulty" only for a certain period of time.  
539 In that case the corrected energy response would be correct for the period when the FEB was  
540 faulty, but would be under-estimated for the period when the FEB behaved "normally". The  
541  $PECorr/cm$  over Plane plot shows the average over these responses.

542 The corrected response across planes in Y view (figure 46) shows a slight incline in the first  
543 half of the detector. We do not know where does this slope come from, but it is not big enough  
544 to be of concern and we decided to ignore it.

545 The distributions of energy deposition in time (figures 54 and 55) show a non-trivial depen-  
546 dency. The detector response could be influenced by environmental factors (temperature and  
547 humidity) and by scintillator or readout ageing. Neither of these factors are well understood  
548 within NOvA and Test Beam detector could be potentially used to shine more light on this  
549 issue. However this is a topic for a separate study and is out of scope of this technical note.

550 Technically, we would expect the distributions of  $PECorr/cm$  to also have the same **scale**  
551 for all data samples and for simulation. As can be seen on all the validation plots, the data  
552 samples have a reasonably similar scale of  $PECorr/cm$ , but this is noticeably different for  
553 simulation. This is caused due to the data-based simulation we are using does not have a correct  
554 energy estimation for through-going muons, which have generally underestimated energies  
555 [28]. This results in an over-estimated correction from the relative calibration. However, this  
556 is not an issue, since we only use stopping muons to calculate the absolute energy scale and  
557 stopping muons have correct energies in the new simulation.

## 558 5 Conclusion

559 We have successfully calibrated the NOvA Test Beam detector for all the Test Beam run periods  
560 in both data and simulation. The calibration results are implemented in the v15.09 version of the  
561 NOvASoft calibration tag. We haven't attempted to estimate the uncertainty of the calibration,  
562 which is a separate task out of scope of this technical note.

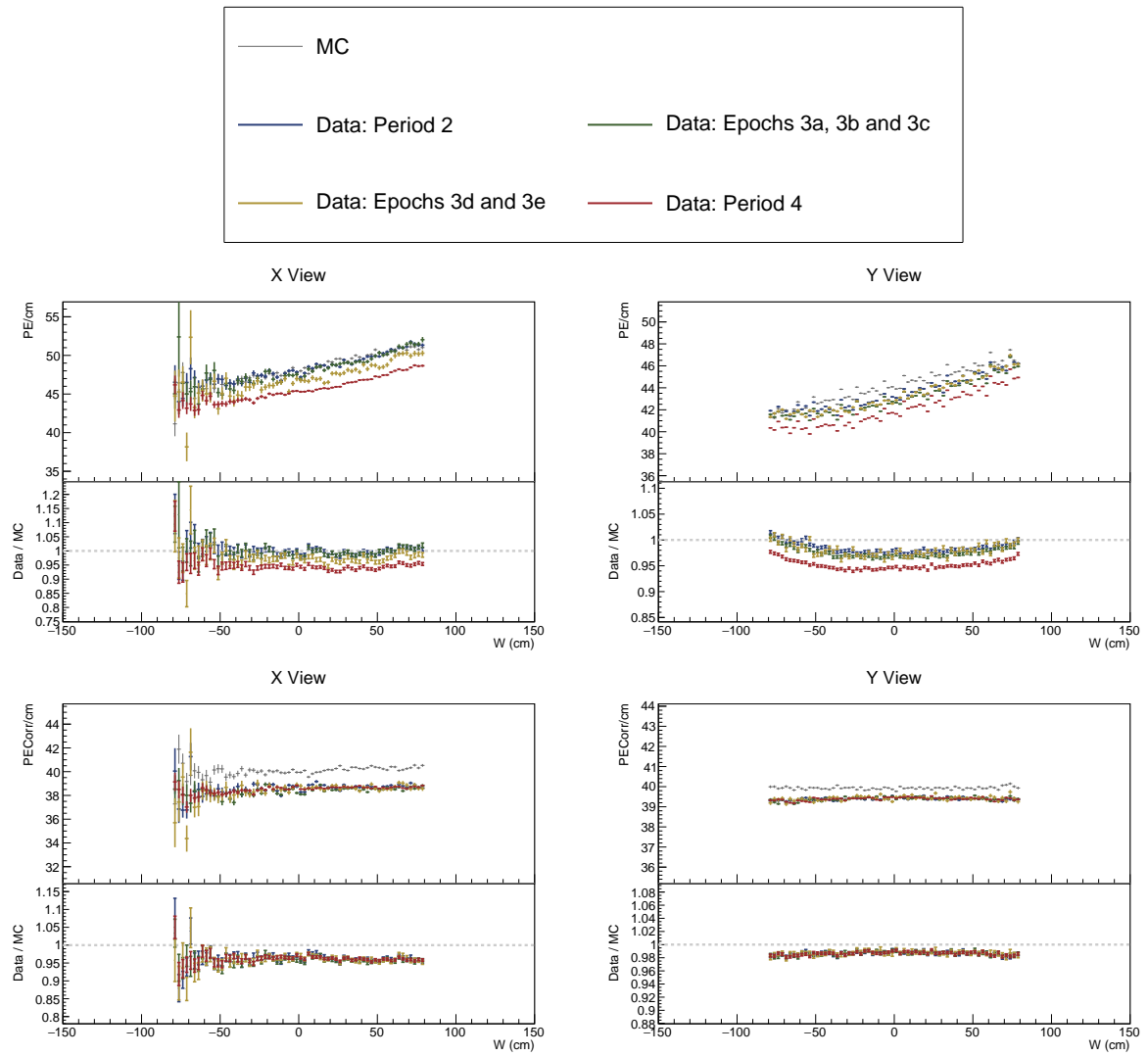


Figure 42: Distributions of stopping muons within a 1-2 m track window from the end of their tracks across the position within a cell.

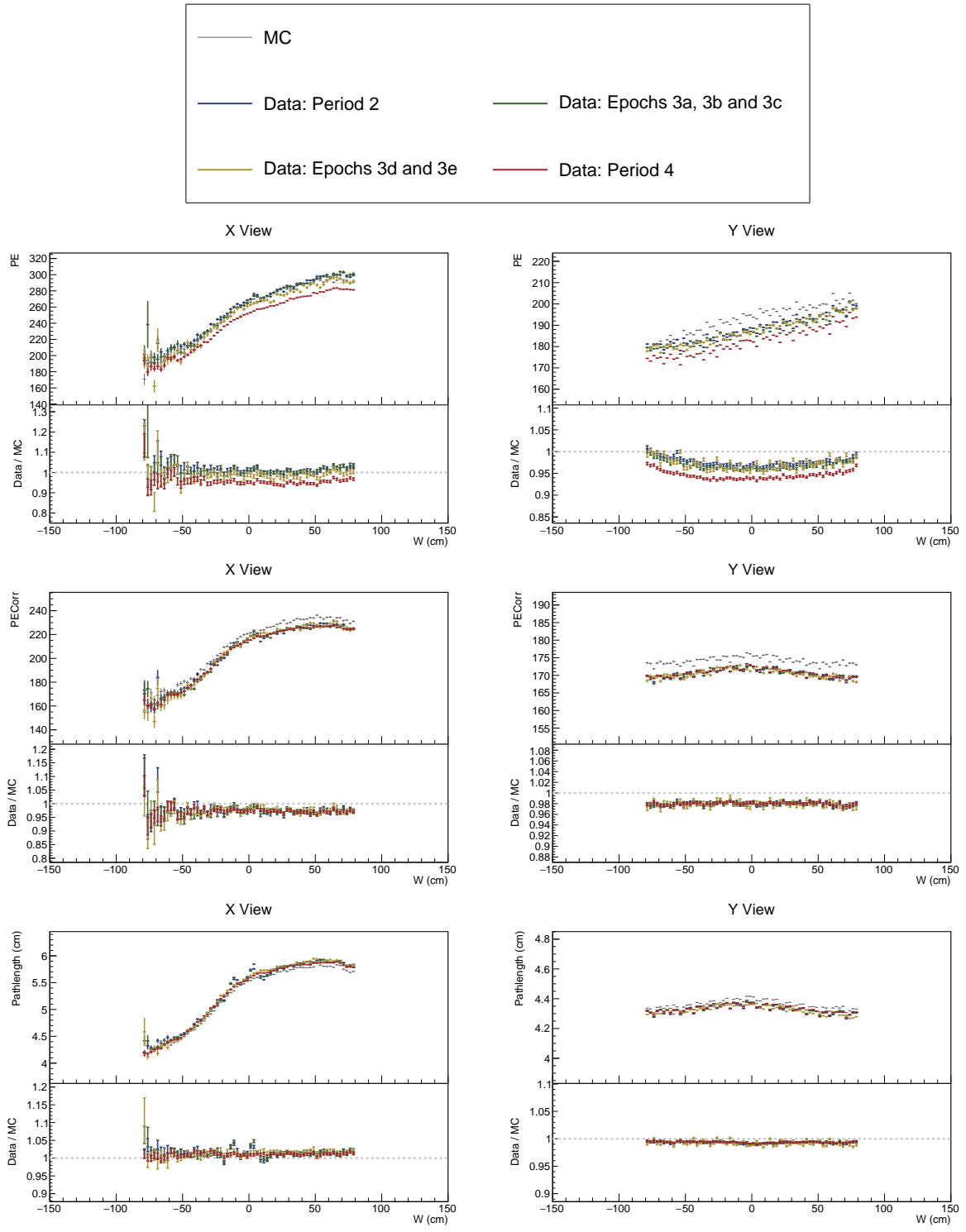


Figure 43: Distributions of stopping muons within a 1-2 m track window from the end of their tracks across the position within a cell.

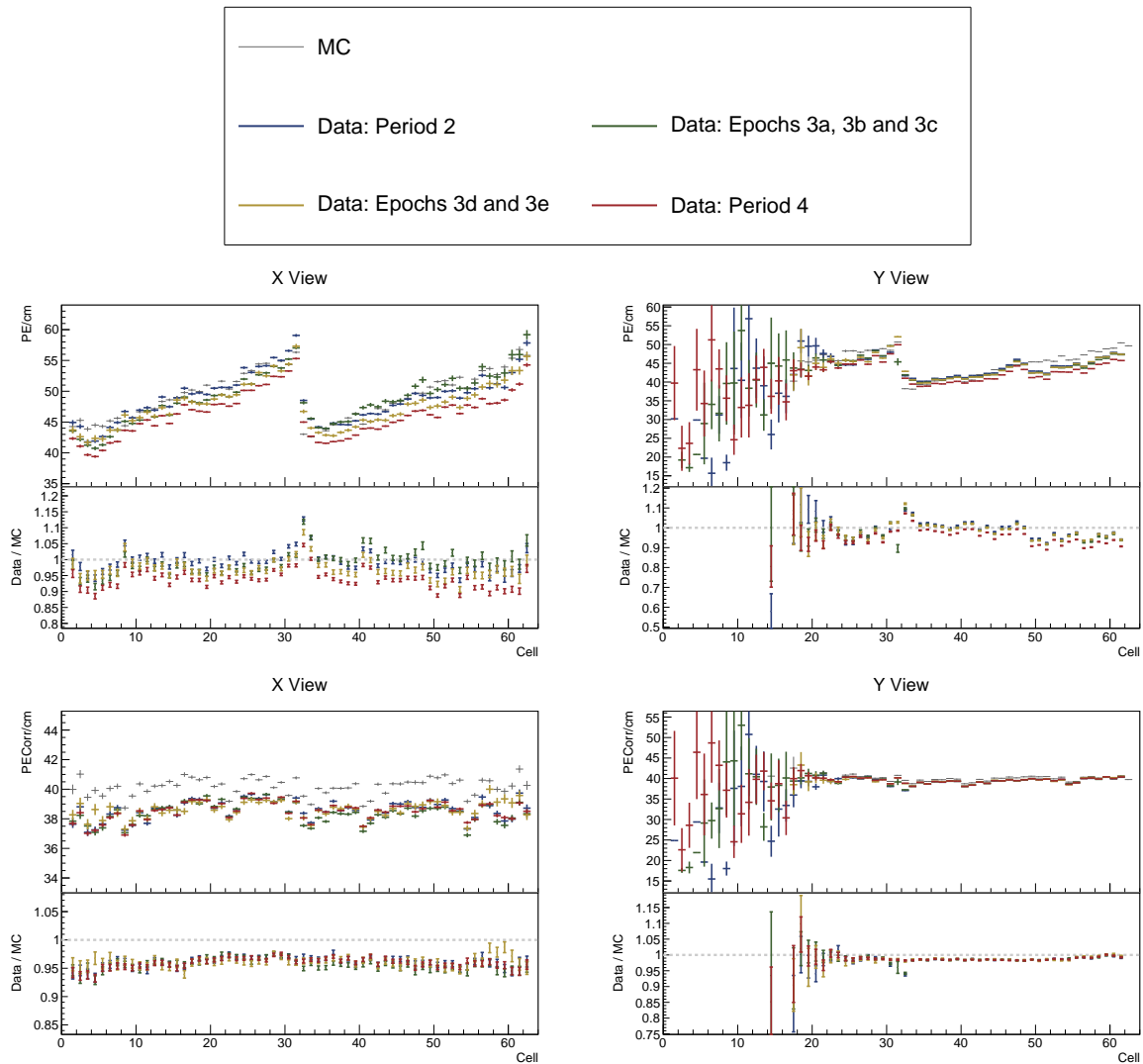


Figure 44: Distributions of stopping muons within a 1-2 m track window from the end of their tracks across the cells of the detector.

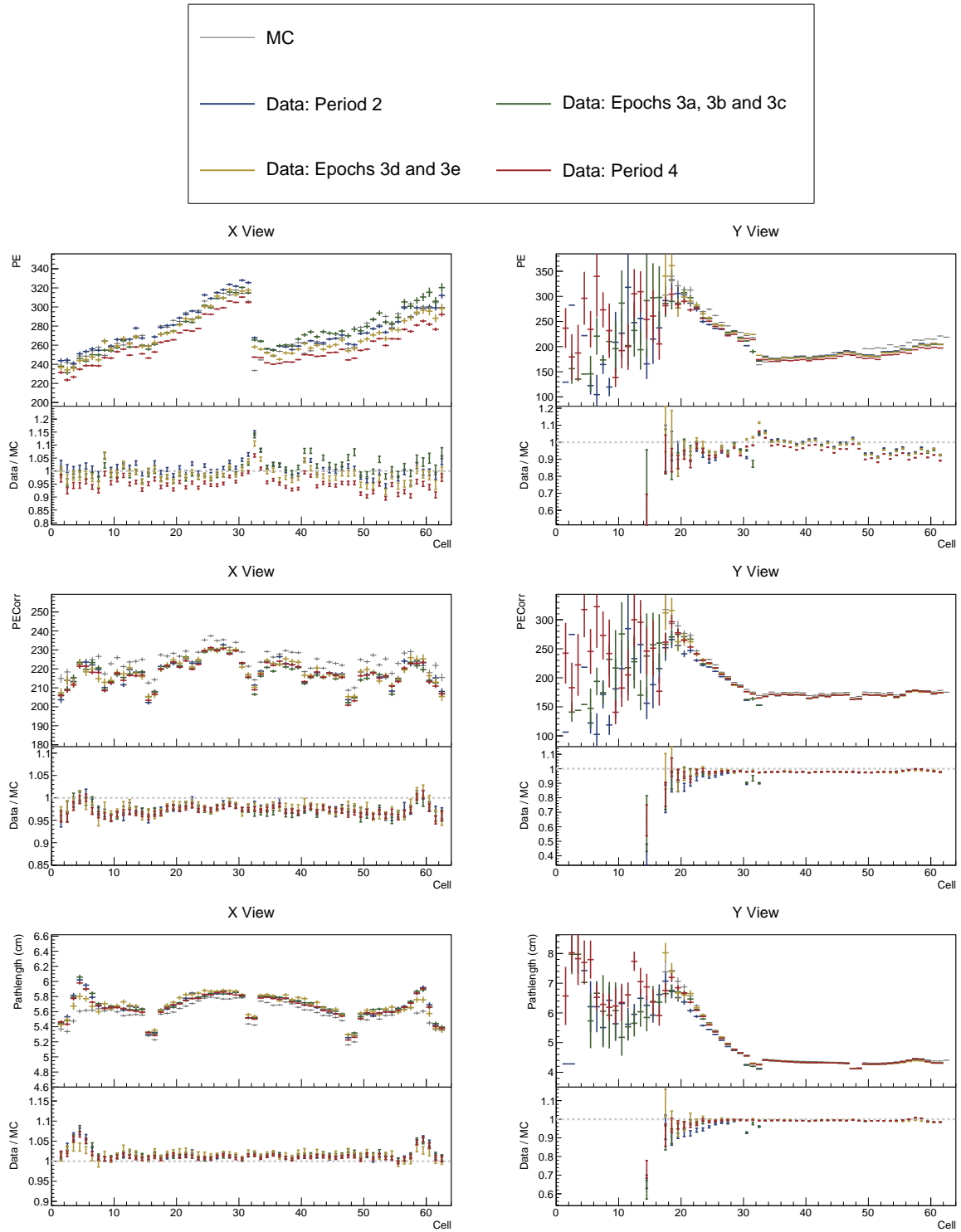


Figure 45: Distributions of stopping muons within a 1-2 m track window from the end of their tracks across the cells of the detector.

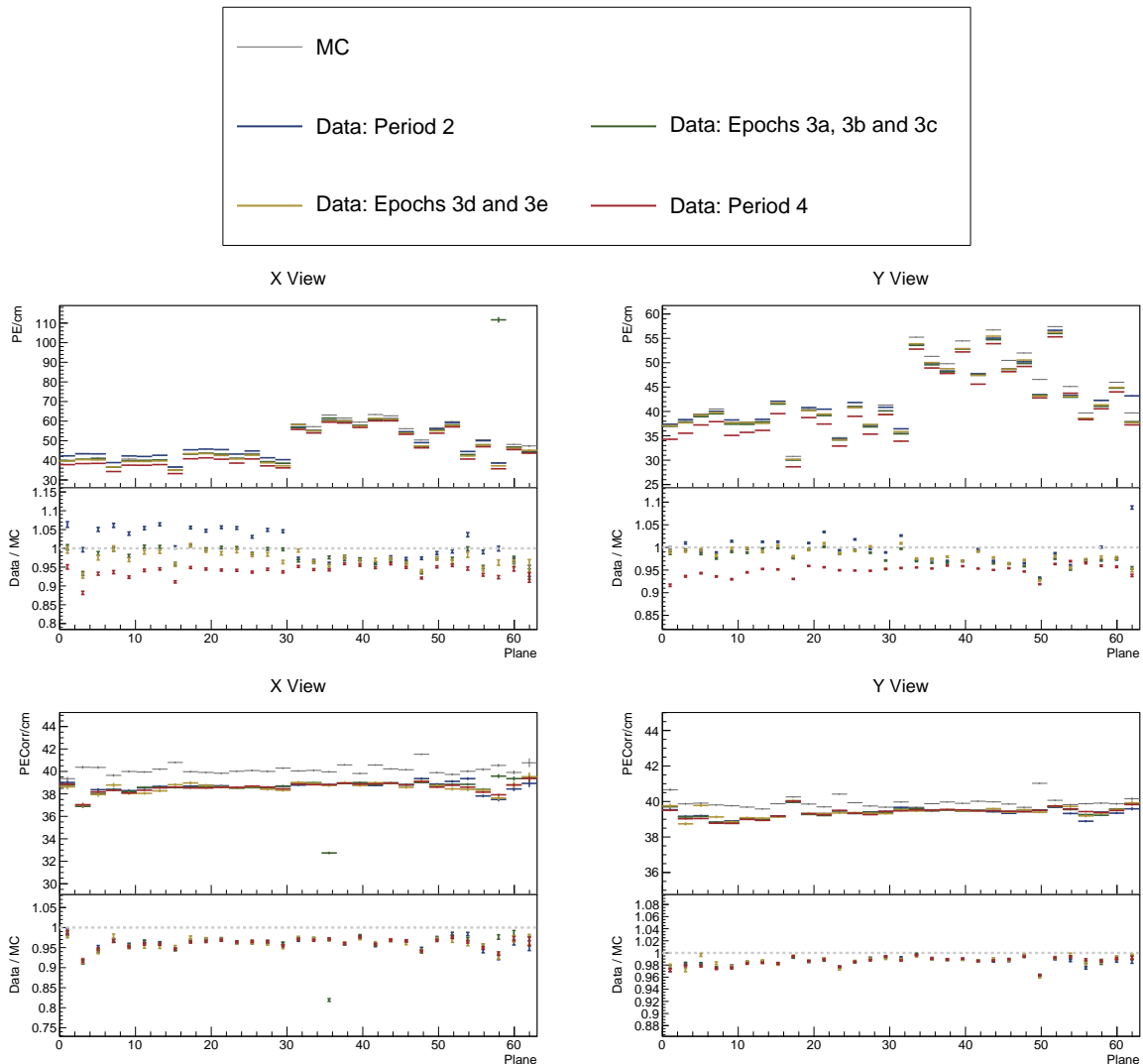


Figure 46: Distributions of stopping muons within a 1-2 m track window from the end of their tracks across the planes of the detector.

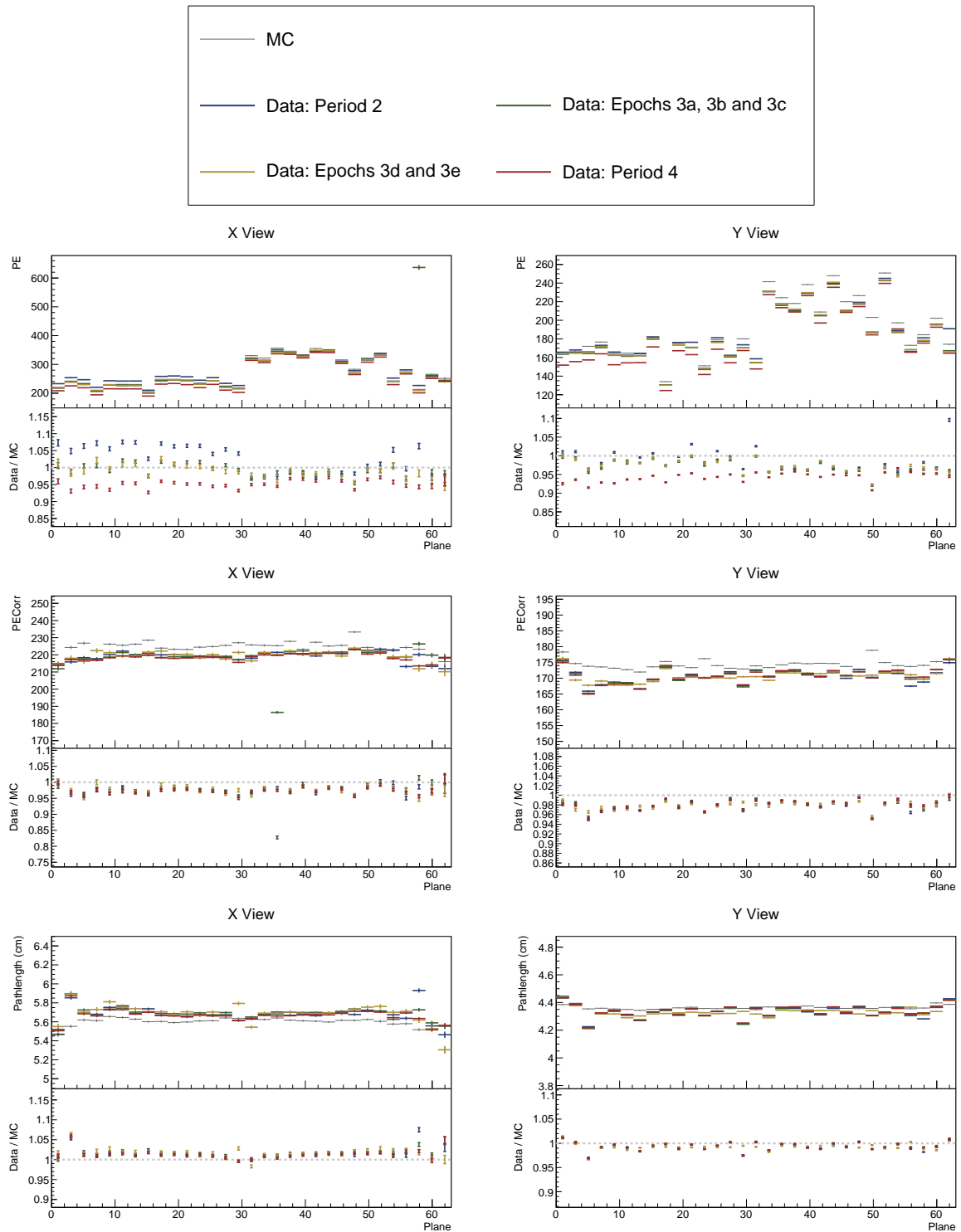


Figure 47: Distributions of stopping muons within a 1-2 m track window from the end of their tracks across the planes of the detector.

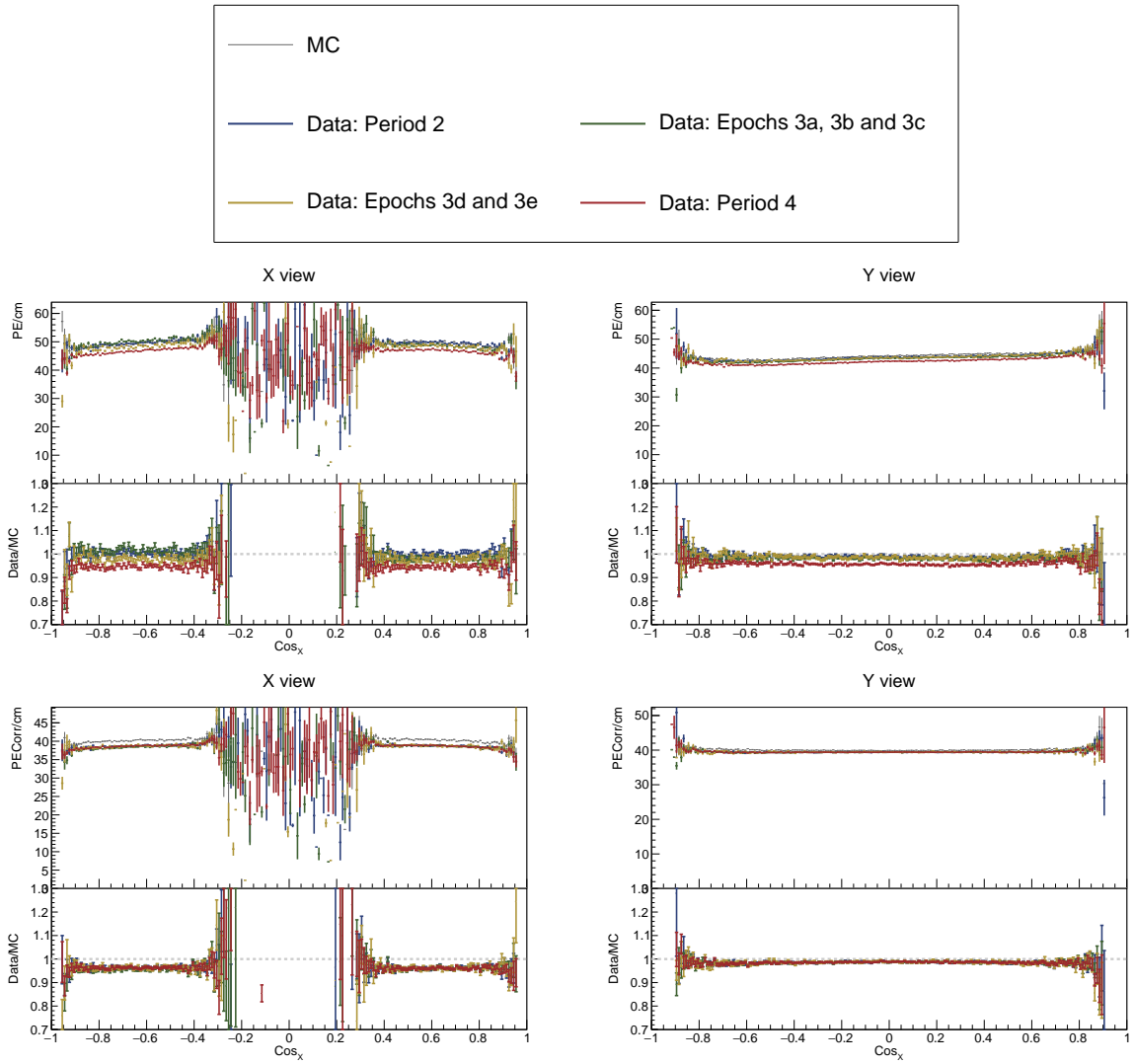


Figure 48: Distributions of stopping muons within a 1-2 m track window from the end of their tracks across the cosine of the track angle from the X (horizontal) axis.

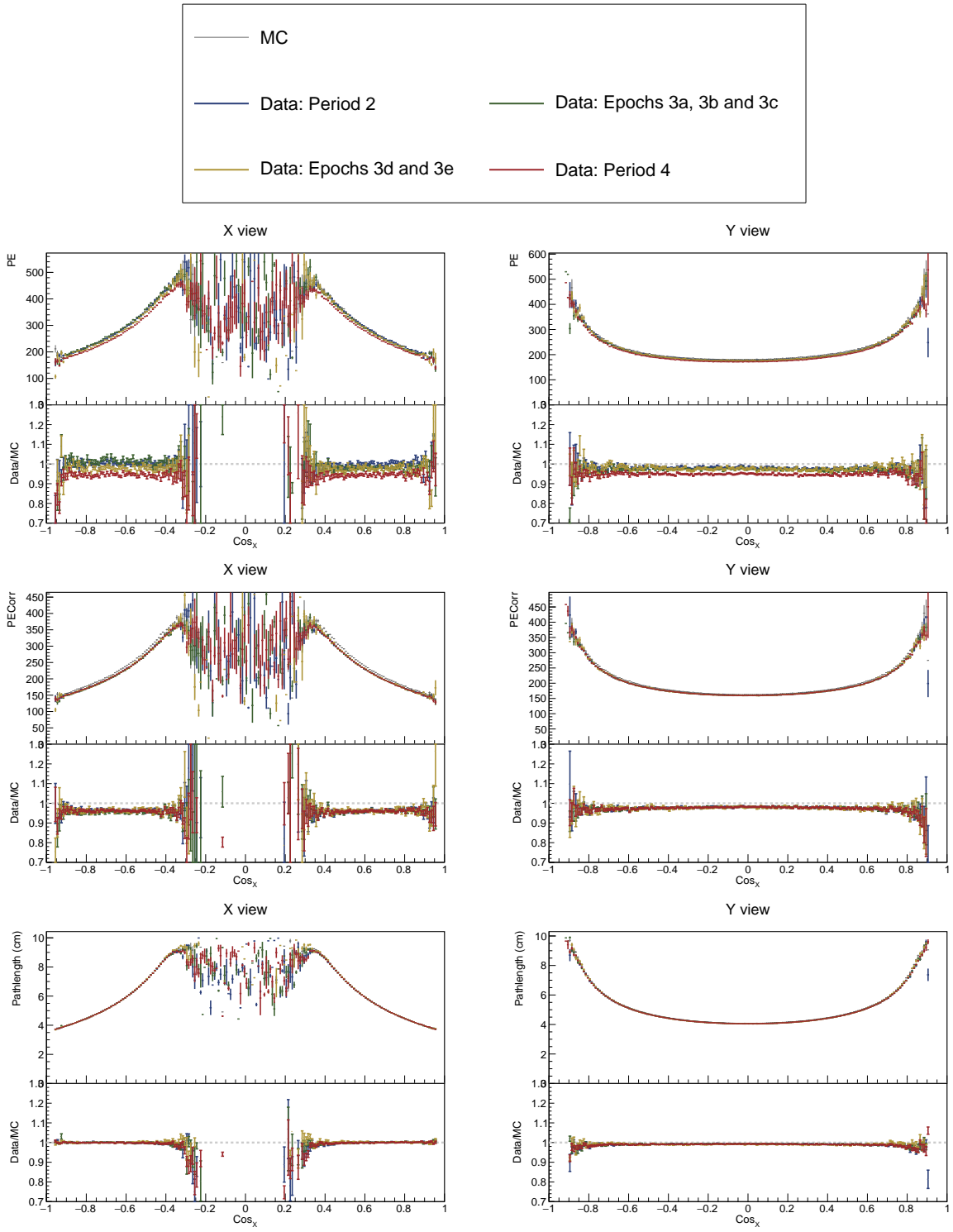


Figure 49: Distributions of stopping muons within a 1-2 m track window from the end of their tracks across the cosine of the track angle from the X (horizontal) axis.

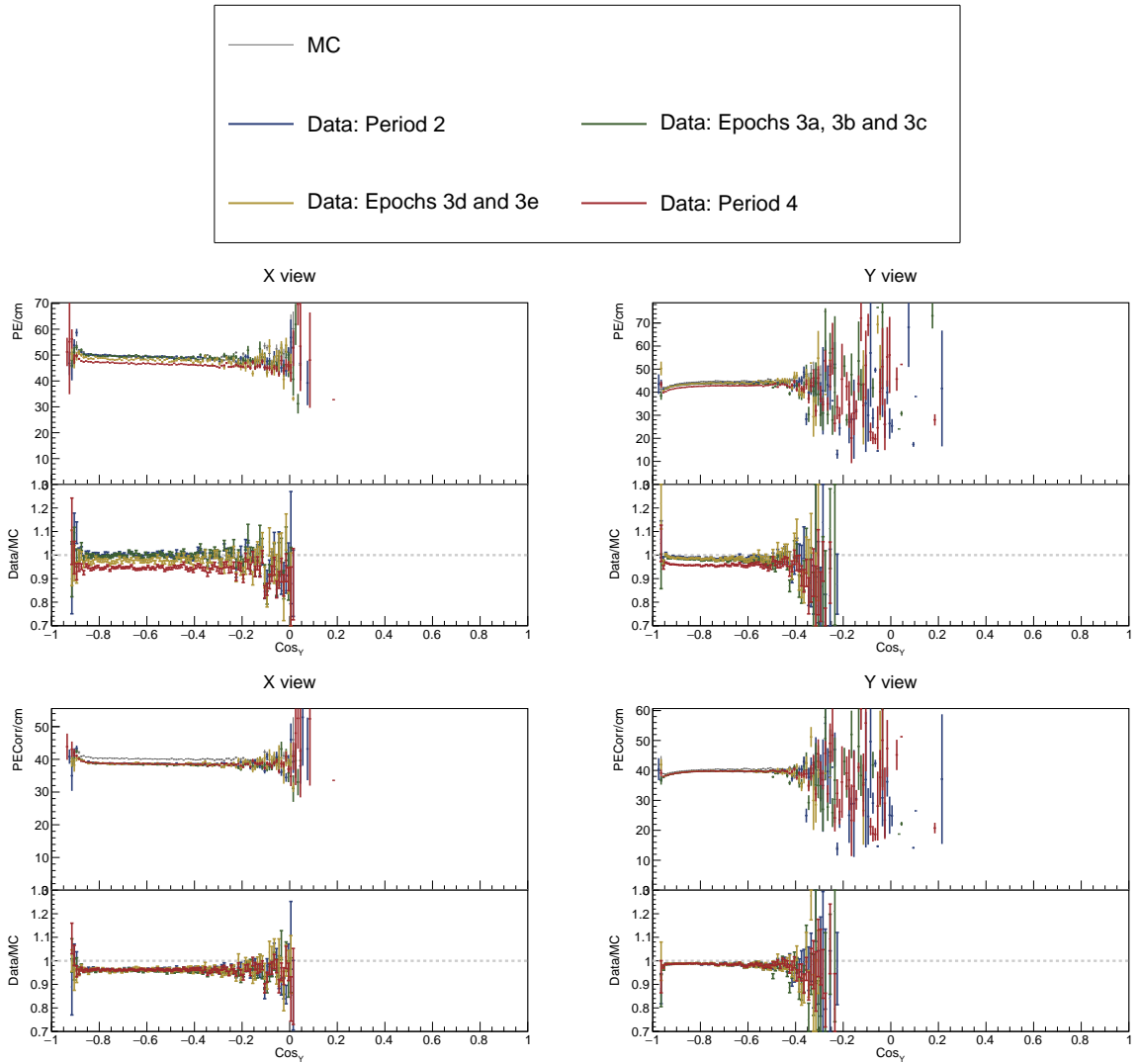


Figure 50: Distributions of stopping muons within a 1-2 m track window from the end of their tracks across the cosine of the track angle from the Y (vertical) axis.

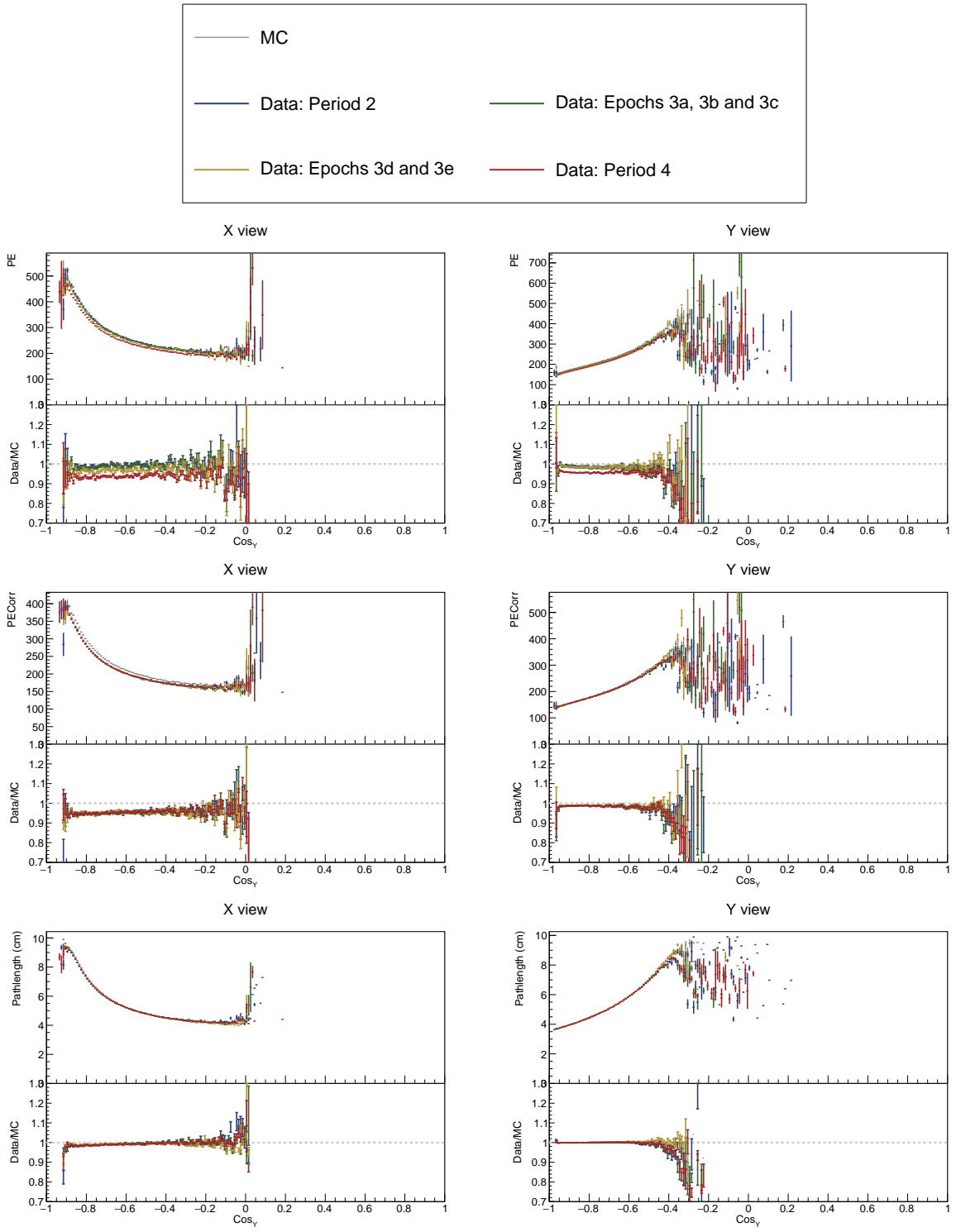


Figure 51: Distributions of stopping muons within a 1-2 m track window from the end of their tracks across the cosine of the track angle from the Y (vertical) axis.

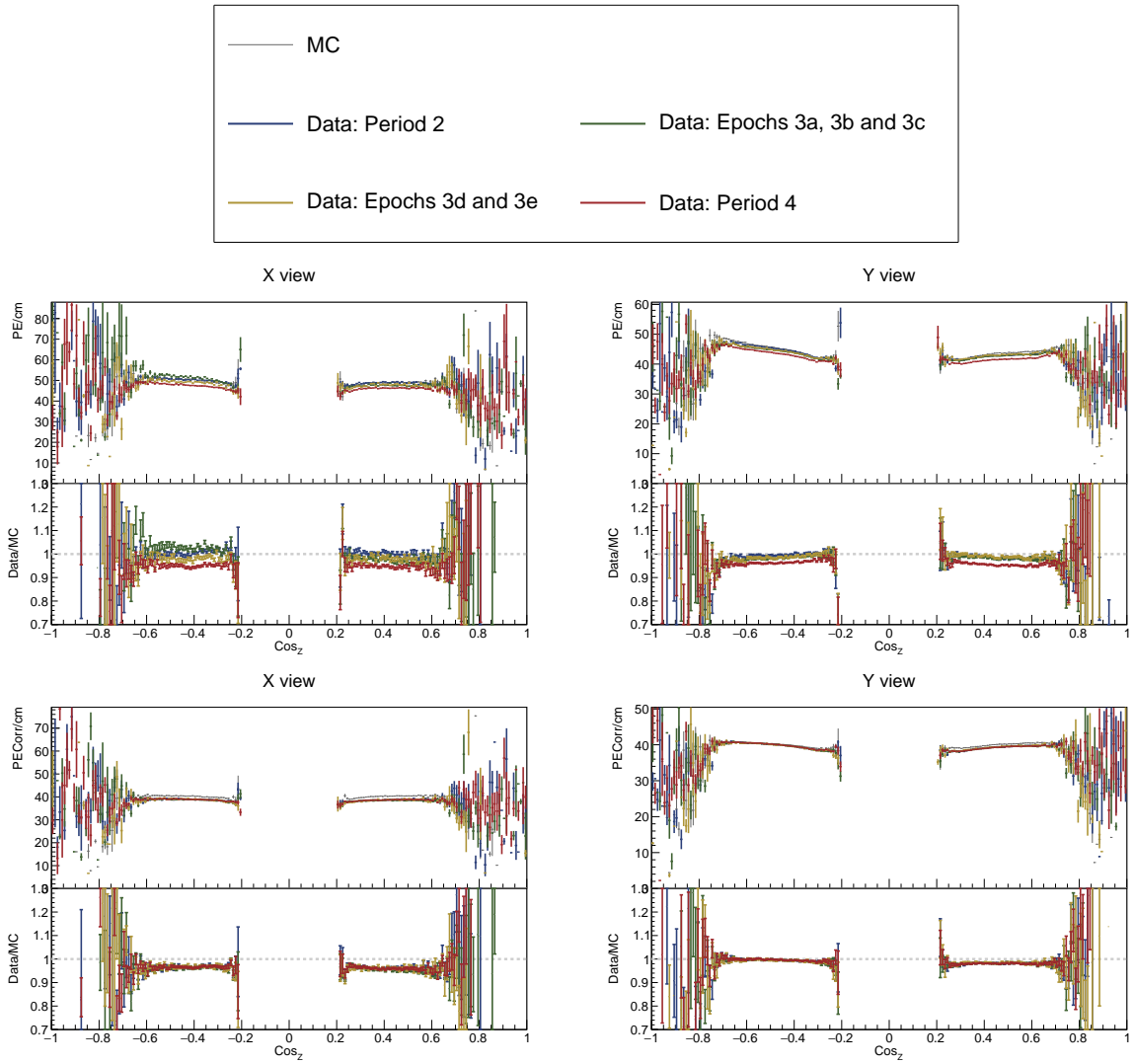


Figure 52: Distributions of stopping muons within a 1-2 m track window from the end of their tracks across the cosine of the track angle from the Z (beam) axis.

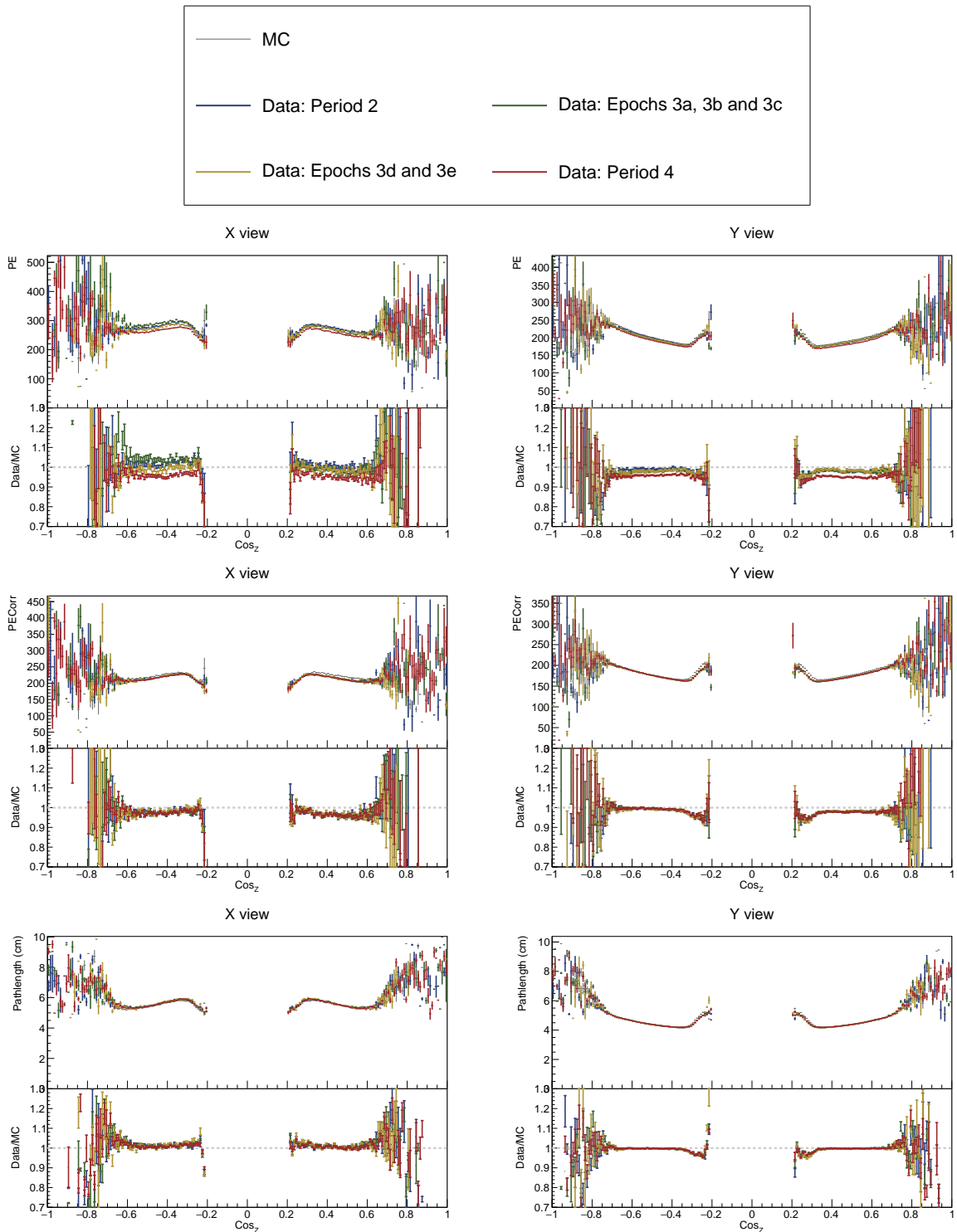


Figure 53: Distributions of stopping muons within a 1-2 m track window from the end of their tracks across the cosine of the track angle from the Z (beam) axis.

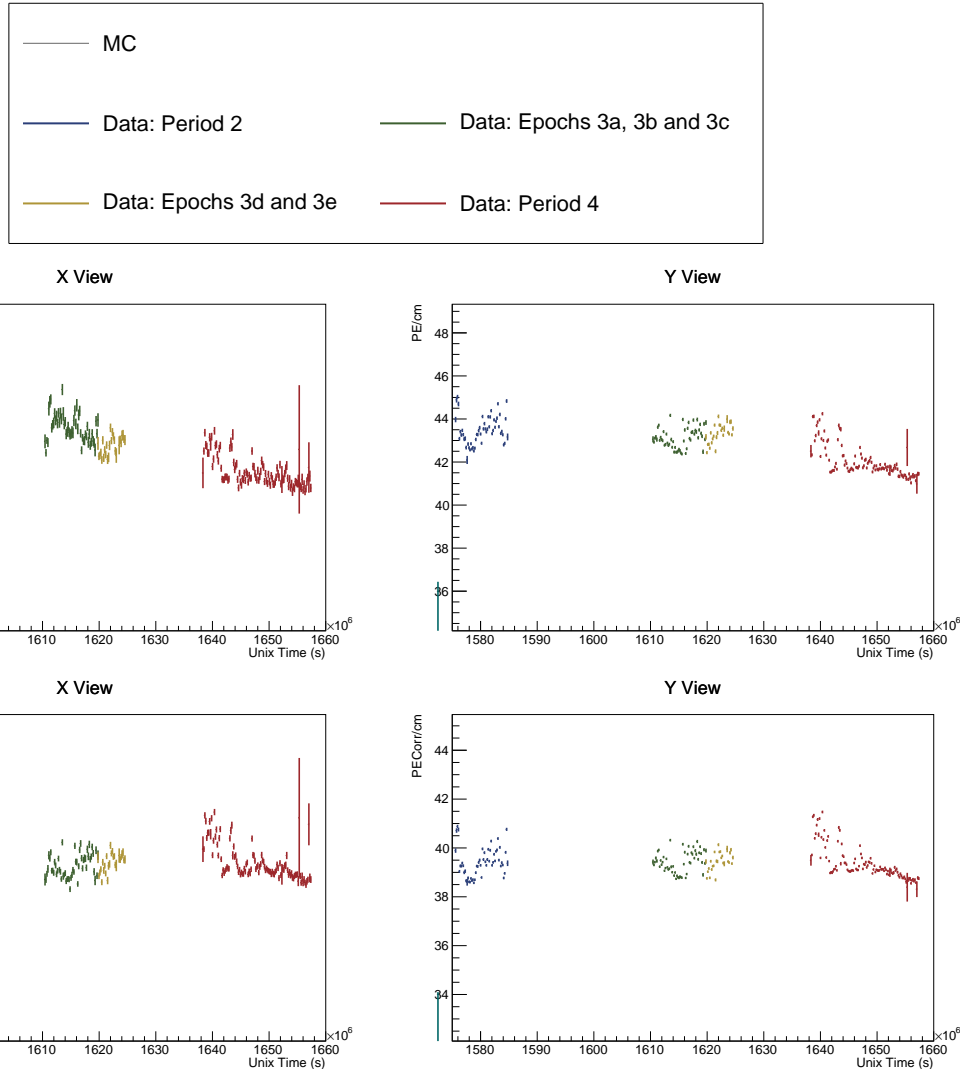


Figure 54: Distributions of stopping muons within a 1-2 m track window from the end of their tracks across the event UNIX time.

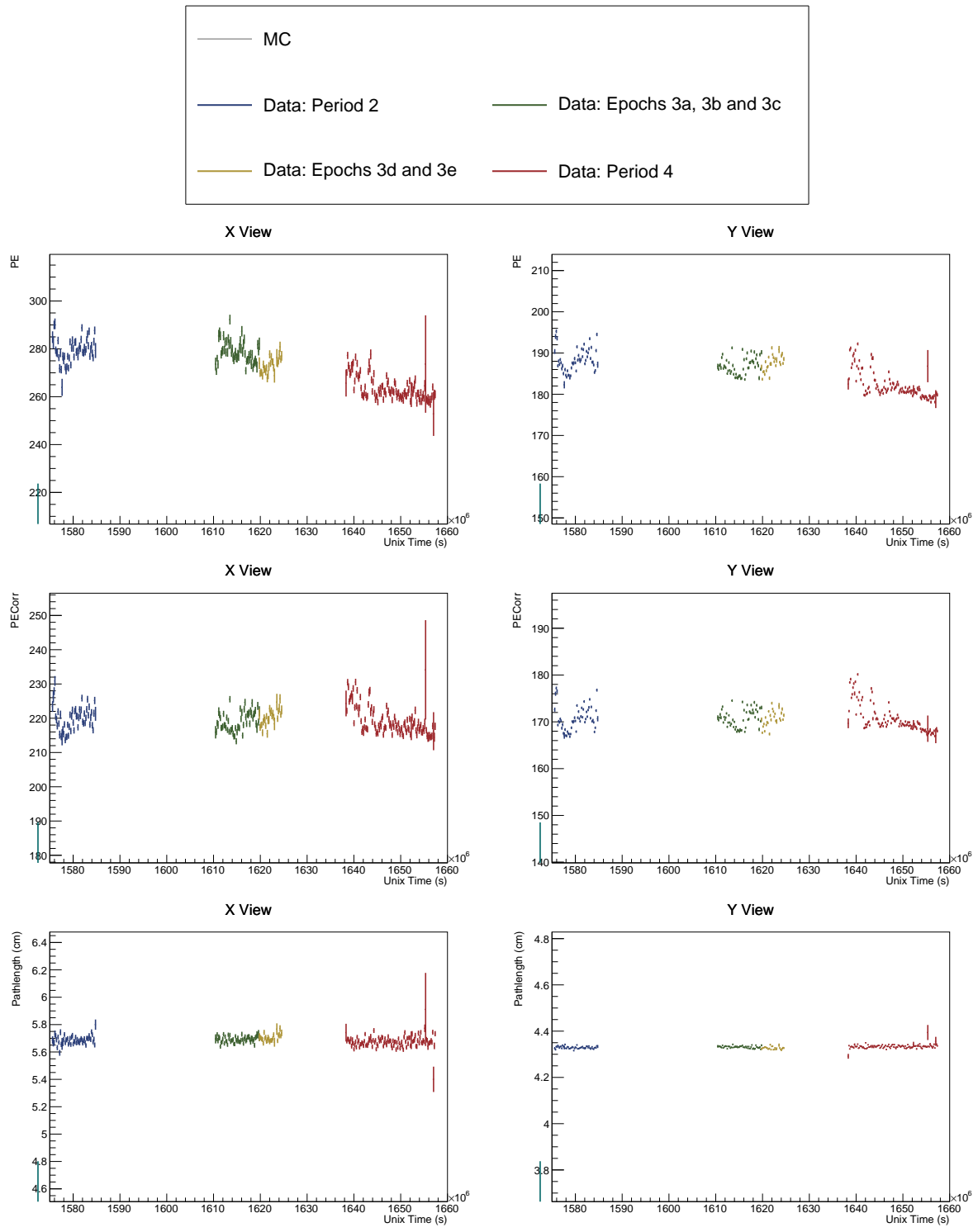


Figure 55: Distributions of stopping muons within a 1-2 m track window from the end of their tracks across the event UNIX time.

563 **References**

- 564 [1] Alex Sousa. Test Beam Plenary Update - FNAL September 2018. NOVA Document  
565 33012, September 2018. NOvA internal document. URL: <https://nova-docdb.fnal.gov/cgi-bin/sso>ShowDocument?docid=33012>.
- 566
- 567 [2] Alex Sousa, Ryan Nichol, Karol Lang, and Jeff Nelson. NOvA Test Beam Task Force  
568 Report. NOVA Document 15750, August 2016. NOvA technical note. URL: <https://nova-docdb.fnal.gov/cgi-bin/sso>ShowDocument?docid=15750>.
- 569
- 570 [3] Kevin Mulder. TB Calibration update. NOVA Document 42700, January 2020.  
571 NOvA internal document. URL: <https://nova-docdb.fnal.gov/cgi-bin/sso>ShowDocument?docid=42700>.
- 572
- 573 [4] Anna Maureen Hall. TB P2 Calib Update. NOVA Document 50786, June 2021.  
574 NOvA internal document. URL: <https://nova-docdb.fnal.gov/cgi-bin/sso>ShowDocument?docid=50786>.
- 575
- 576 [5] Robert Kralik. Test Beam calibration results - Spring 2023. NOVA Document 59024, June  
577 2023. NOvA internal document. URL: <https://nova-docdb.fnal.gov/cgi-bin/sso>ShowDocument?docid=59024>.
- 578
- 579 [6] Alex Sousa. NOvA Test Beam Status and Plans - Support Documentation. NOVA Doc-  
580 ument 22172-v2, October 2017. NOvA technical note. URL: <https://nova-docdb.fnal.gov/cgi-bin/sso>ShowDocument?docid=22172>.
- 581
- 582 [7] Alex Sousa. NOvA Test Beam Plenary @ IU Collaboration Meeting. NOVA Document  
583 29543, May 2018. NOvA internal document. URL: <https://nova-docdb.fnal.gov/cgi-bin/sso>ShowDocument?docid=29543>.
- 584
- 585 [8] Michael Wallbank. Final Test Beam Updates (Geometry and Other!). NOVA Document  
586 58388, April 2023. NOvA internal document. URL: <https://nova-docdb.fnal.gov/cgi-bin/sso>ShowDocument?docid=58388>.
- 587
- 588 [9] Michael Wallbank. Understanding, Improving, Validating the Test Beam Geometry.  
589 NOVA Document 57955, February 2023. NOvA internal document. URL: <https://nova-docdb.fnal.gov/cgi-bin/sso>ShowDocument?docid=57955>.
- 590
- 591 [10] Robert Kralik. Test beam calibration update. NOVA Document 57516-v2, January  
592 2023. NOvA internal document. URL: <https://nova-docdb.fnal.gov/cgi-bin/sso>ShowDocument?docid=57516>.
- 593
- 594 [11] Alex Sousa. Test Beam Plenary Update - Jun. 6, 2019. NOVA Document 38349, June  
595 2019. NOvA internal document. URL: <https://nova-docdb.fnal.gov/cgi-bin/sso>ShowDocument?docid=38349>.
- 596
- 597 [12] Alex Sousa. Filling System and Scintillator Status. NOVA Document 34067, November  
598 2018. NOvA internal document. URL: <https://nova-docdb.fnal.gov/cgi-bin/sso>ShowDocument?docid=34067>.
- 599

- 600 [13] Junting Huang, Will Flanagan, and Beatriz Tapia Oregui. Test Beam: Light Yield of  
601 the Liquid Scintillator Drained from the NDOS Detector. NOVA Document 38740, July  
602 2019. NOvA internal document. URL: <https://nova-docdb.fnal.gov/cgi-bin/sso>ShowDocument?docid=38740>.
- 604 [14] Dung Phan. Test Beam: Tintometer Measurement of Texas A&M oil. NOVA Document  
605 39088, July 2019. NOvA internal document. URL: <https://nova-docdb.fnal.gov/cgi-bin/sso>ShowDocument?docid=39088>.
- 607 [15] Alex Sousa. Test Beam Scintillator Fill Plan. NOVA Document 34196, November  
608 2018. NOvA internal document. URL: <https://nova-docdb.fnal.gov/cgi-bin/sso>ShowDocument?docid=34196>.
- 610 [16] Alex Sousa. 2nd Block Filling Status - Nov. 18, 2019. NOVA Document 41961, November  
611 2019. NOvA internal document. URL: <https://nova-docdb.fnal.gov/cgi-bin/sso>ShowDocument?docid=41961>.
- 613 [17] Teresa Megan Lackey. *Proton Scattering in NOvA Test Beam*. PhD thesis, Indiana U.,  
614 July 2022.
- 615 [18] David Northacker, Alex Sousa, and Yagmur Torun. Test Beam - Overfilling Horizontal  
616 Planes. NOVA Document 49439, March 2021. NOvA internal document. URL: <https://nova-docdb.fnal.gov/cgi-bin/sso>ShowDocument?docid=49439>.
- 618 [19] Keith Matera et al. Calibration Technotes. NOVA Document 13579, January  
619 2017. NOvA technical note. URL: <https://nova-docdb.fnal.gov/cgi-bin/sso>ShowDocument?docid=13579>.
- 621 [20] Christopher J. Backhouse. Cell-by-cell attenuation calibration of the NOvA detectors.  
622 NOVA Document 7410, December 2014. NOvA technical note. URL: <https://nova-docdb.fnal.gov/cgi-bin/sso>ShowDocument?docid=7410>.
- 624 [21] Evan David Niner. *Observation of Electron Neutrino Appearance in the NuMI Beam with  
625 the NOvA Experiment*. PhD thesis, Indiana U., 2015. doi:10.2172/1221353.
- 626 [22] Christopher J. Backhouse. Timing bias introduced by incorrect interpretation of the  
627 nanoslice. NOVA Document 13518, June 2015. NOvA technical note. URL: <https://nova-docdb.fnal.gov/cgi-bin/sso>ShowDocument?docid=13518>.
- 629 [23] Luke Vinton. Calorimetric Energy Scale Calibration of the NOvA Detectors. NOVA Doc-  
630 ument 13579, document FA\_Calorimetric\_energy\_scale.pdf, July 2015. NOvA technical  
631 note. URL: <https://nova-docdb.fnal.gov/cgi-bin/sso>ShowDocument?docid=13579>.
- 633 [24] Keith Matera. Keith's Swell Guide: The Calibration Meta. NOVA Document 13579, doc-  
634 ument Calibration\_Meta\_READFIRST.pdf, January 2017. NOvA technical note. URL:  
635 <https://nova-docdb.fnal.gov/cgi-bin/sso>ShowDocument?docid=13579>.

- 636 [25] Christopher Backhouse, Alexender Radovic, and Prabhjot Singh. The Attenuation and  
637 Threshold Calibration of the NOvA detectors. NOVA Document 13579, document  
638 SA\_Attenuation\_and\_Threshold.pdf, May 2016. NOvA technical note. URL: <https://nova-docdb.fnal.gov/cgi-bin/sso>ShowDocument?docid=13579>.
- 640 [26] Ryan J. Nichol. Fibre brightness from cosmic muon data. NOVA Document 34909, De-  
641 cember 2018. NOvA technical note. URL: <https://nova-docdb.fnal.gov/cgi-bin/sso>ShowDocument?docid=34909>.
- 643 [27] Alex Sousa. Test Beam Plenary Update, Oct. 2019. NOVA Document 41331, October  
644 2019. NOvA internal document. URL: <https://nova-docdb.fnal.gov/cgi-bin/sso>ShowDocument?docid=41331>.
- 646 [28] Robert Kralik. Data-based simulation of cosmic muons (not only) for calibration. NOVA  
647 Document 60026, October 2023. NOvA technical note. URL: <https://nova-docdb.fnal.gov/cgi-bin/sso>ShowDocument?docid=60026>.
- 649 [29] Anna Maureen Hall. TB P2 Calib. Summary. NOVA Document 49674, March 2021.  
650 NOvA internal document. URL: <https://nova-docdb.fnal.gov/cgi-bin/sso>ShowDocument?docid=49674>.
- 652 [30] Matthew Strait. Update on light level tuning. NOVA Document 43249, February  
653 2020. NOvA internal document. URL: <https://nova-docdb.fnal.gov/cgi-bin/sso>ShowDocument?docid=43249>.
- 655 [31] Artur Sztuc. DCM/FEB Shut-Off Studies. NOVA Document 53658, February 2022.  
656 NOvA internal document. URL: <https://nova-docdb.fnal.gov/cgi-bin/sso>ShowDocument?docid=53658>.
- 658 [32] Lisa W Koerner and Ryan J Nichol. Executive summary of calibration for the 2019  
659 analyses. NOVA Document 36915, May 2019. NOvA technical note. URL: <https://nova-docdb.fnal.gov/cgi-bin/sso>ShowDocument?docid=36915>.
- 661 [33] Lisa W Koerner. Calibration Tagging. NOVA Document 59268, June 2023.  
662 NOvA internal document. URL: <https://nova-docdb.fnal.gov/cgi-bin/sso>ShowDocument?docid=59268>.